

Nucleon Electromagnetic Form Factors

Haiyan Gao

*Triangle University Nuclear Laboratory and Department of Physics, Duke University
Durham, North Carolina 27708, U.S.A.
Laboratory for Nuclear Science and Department of Physics, Massachusetts Institute of Technology
Cambridge, Massachusetts 02139, U.S.A.
gao@tunl.duke.edu*

Nucleon electromagnetic form factors are fundamental quantities related to the charge and magnetization distributions inside the nucleon. Understanding the nucleon electromagnetic structure in terms of the underlying quark and gluon degrees of freedom of quantum chromodynamics is a challenging and urgent task. The nucleon electromagnetic form factors have been studied in the past extensively from unpolarized electron scattering experiments. With the development in polarized beam, recoil polarimetry, and polarized target technologies, polarization experiments have provided more precise data on these quantities. At the same time, significant theoretical progress in areas ranging from effective field theories to lattice QCD calculations, has been made in describing these data. In this article, I review recent experimental and theoretical progress on this subject. I will also provide future outlook on this topic.

1. Introduction

Nucleons (protons and neutrons) are fundamental building blocks of matter. Nevertheless, they are not fundamental particles. Otto Stern received the Nobel Prize in Physics in 1943, for his experimental methods of studying the magnetic properties of nuclei, in particular for measuring the magnetic moment of the proton itself. The anomalous magnetic moments of the proton and neutron reveal that nucleons are not point-like Dirac particles, but particles with underlying structure.

The electromagnetic form factors of the nucleon have been a longstanding subject of interest in nuclear and particle physics. They are fundamental quantities describing the distribution of charge and magnetization within nucleons. Probing the nucleon electromagnetic structure has been an ongoing experimental endeavor since the discovery of the anomalous magnetic moment of the proton.

Electron scattering has been proven to be a very useful tool in probing the structure of nucleon and nuclei. The leptonic part of the vertex is well understood from Quantum Electrodynamics (QED), thus it is a clean probe of hadronic structure. Furthermore, the electromagnetic coupling constant is relatively weak, so higher order diagrams are suppressed compared to the lowest order one-photon-exchange

diagram. The study of the electromagnetic structure of the proton from electron-proton elastic scattering was pioneered by Hofstadter and colleagues at the Stanford Linear Accelerator Center (SLAC) in the 1950s, for which Hofstadter received the Nobel Prize in Physics in 1961. The deep-inelastic scattering experiments of electrons from protons carried out by Friedman, Kendall and Taylor which established the underlying quark structure of the proton at SLAC, led to the Nobel Prize in Physics in 1990.

Quantum Chromodynamics (QCD) is the theory of strong interaction in terms of quark and gluon degrees of freedom. While QCD has been extremely well tested in the high energy regime, where perturbative QCD is applicable, understanding confinement and hadron structure in the non-perturbative region of QCD remains challenging. Knowledge of the internal structure of protons and neutrons in terms of quark and gluon degrees of freedom is not only essential for testing QCD in the confinement regime, but it also provides a basis for understanding more complex, strongly interacting matter at the level of quarks and gluons.

The rest of the paper is organized as follows: Section II gives an introduction on the nucleon electromagnetic form factors; Section III contains a discussion on form factor data from unpolarized electron scattering experiments; Section IV presents recent data on the nucleon electromagnetic form factors from double-polarization experiments; Section V reviews theoretical progress on the nucleon electromagnetic form factors; and Section VI provides future outlook on this subject.

2. The Nucleon Electromagnetic Form Factors

From QED, the lowest-order amplitude (Fig. 1) for electron-nucleon elastic scattering is given by

$$T_{fi} = -i \int j_\mu \left(\frac{-1}{q^2} \right) J^\mu d^4x, \quad (1)$$

where $q = p' - p$ and the electron transition current is

$$j^\mu = -e \bar{u}(k') \gamma^\mu u(k) e^{i(k' - k) \cdot x} \quad (2)$$

The nucleon is an extended spin- $\frac{1}{2}$ object, thus the nucleon transition current is more complicated than that of the electron. Based on the requirements of covariance under the improper Lorentz group, current conservation and parity conservation, the nucleon transition current is written as

$$J^\mu = e \bar{u}(p') \left[F_1(q^2) \gamma^\mu + \frac{\kappa}{2M} F_2(q^2) i \sigma^{\mu\nu} q_\nu \right] u(p) e^{i(p' - p) \cdot x}, \quad (3)$$

where F_1 and F_2 are two independent form factors, also called the Dirac and Pauli form factors, respectively, κ is the anomalous magnetic moment, and M is the nucleon mass.

Ernst, Sachs, and Wali¹ defined the following, the so-called Sachs' form factors: $G_E(q^2)$ (electric form factor) and $G_M(q^2)$ (magnetic form factor), which are written

as linear combinations of F_1 and F_2 :

$$G_E = F_1 + \frac{\kappa q^2}{4M^2} F_2, \quad (4)$$

$$G_M = F_1 + \kappa F_2. \quad (5)$$

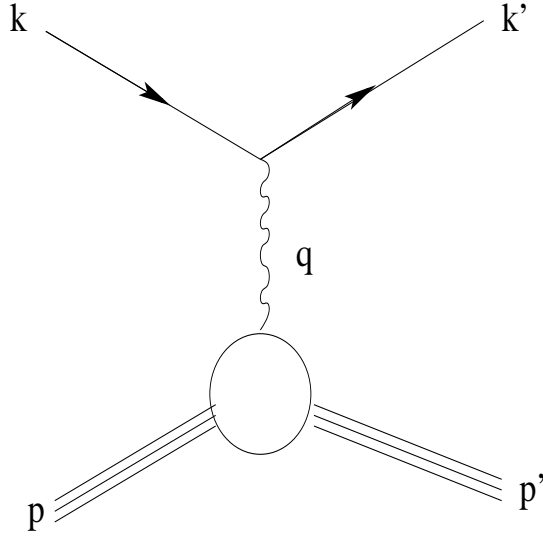


Fig. 1. The one-photon-exchange diagram for electron-nucleon elastic scattering.

The Sachs' form factors, G_E and G_M , have more intuitive physical interpretations than F_1 and F_2 . In electron scattering, the inverse of the four-momentum transfer squared, Q^2 ($Q^2 = -q^2 \geq 0$) is commonly used. In the limit of $Q^2 = 0$,

$$G_E^p(Q^2 = 0) = 1, G_E^n(Q^2 = 0) = 0$$

and

$$G_M^p(Q^2 = 0) = \mu_p, G_M^n(Q^2 = 0) = \mu_n,$$

corresponding to the charge and the magnetic moment of the nucleon, respectively. Sachs² demonstrated that G_E and G_M can be interpreted as Fourier transforms of spatial distributions of charge and magnetization of the nucleon in the so-called Breit frame. For elastic electron-nucleon scattering, the Breit frame coincides with the center-of-mass frame of the electron-nucleon system. In this reference frame, the incoming electron has a momentum of $\frac{\vec{q}}{2}$ and the nucleon initial momentum is $-\frac{\vec{q}}{2}$; the scattered electron has a momentum of $-\frac{\vec{q}}{2}$ and the recoil proton has a momentum of $\frac{\vec{q}}{2}$. Thus, the Breit frame is a special Lorentz frame in which $q^2 = -\vec{q}^2$, i.e., no energy transfer is involved in this particular reference frame. Thus, for each q^2 value, there is a Breit frame in which the form factors are represented as

$G_{E,M}(\vec{q}^2) = G_{E,M}(q^2)$, where $G_{E,M}(q^2)$ is determined in the lab frame. One can therefore perform a three-dimensional Fourier transformation once the form factor information is available,

$$\rho(\vec{r}) = \int \frac{d^3q}{2\pi^3} e^{-i\vec{q}\cdot\vec{r}} \frac{M}{E(\vec{q})} G_E(\vec{q}^2). \quad (6)$$

Although relativity obscures the physical interpretation of such a quantity, it is analogous to the “classical” charge density distribution.

In the low q^2 region, below the two-pion production threshold (i.e., $q^2 < t_0$, where $t_0 = (2m_\pi)^2 < 2 \text{ fm}^{-2}$) the energy transfer in the scattering process is negligible and nucleon electric and magnetic form factors can be taken as the Fourier transforms of the charge and magnetization radial distributions $\rho_{\text{chg}}(r)$ and $\rho_{\text{mag}}(r)$ in the rest frame of the nucleon.

In the non-relativistic limit, the root-mean-square (rms) charge radius of the nucleon is related to the nucleon electric form factor as:

$$\frac{\langle r^2 \rangle}{6} = - \left. \frac{dG_E(Q^2)}{dQ^2} \right|_{Q^2=0}, \quad (7)$$

with the boundary condition $G_E(Q^2 = 0) = 1$ for the proton and 0 for the neutron. The corresponding rms magnetic radius is

$$\frac{\langle r^2 \rangle}{6} = - \frac{1}{\mu_N} \left. \frac{dG_M(Q^2)}{dQ^2} \right|_{Q^2=0}, \quad (8)$$

where μ_N is the nucleon magnetic moment, $\mu_p = 2.79$ and $\mu_n = -1.91$, in the units of the nucleon magneton.

Recent results from lattice QCD calculations^{3,4} suggest that the nucleon rms charge radius can be calculated from first principles with an uncertainty of only a few percent, and this field is rapidly evolving due to both improvements in computer architecture and new algorithms. Thus, precise information on this fundamental quantity is essential in terms of testing the QCD prediction from the lattice.

Accurate information about the proton charge radius is also essential in conducting high-precision tests of QED from hydrogen Lamb shift measurements. The standard Lamb shift measurement probes the 1057 MHz fine structure transition between the $2S_{1/2}$ and $2P_{1/2}$ states in hydrogen. The hydrogen Lamb shift can be calculated to high precision from QED using higher order corrections. The proton rms charge radius is an important input in calculating the hadronic contribution to the hydrogen Lamb shift.

The two most precise and widely cited determinations of the proton charge radius from electron scattering experiments in the literature give $r_p = 0.805(11) \text{ fm}$ ⁵ and $r_p = 0.862(12) \text{ fm}$ ⁶, respectively, differing from each other by more than 7%. While the recent precision hydrogen Lamb shift measurements^{7,8,9,10,11} are in better agreement with the QED predictions using the smaller value of the proton charge radius without the two-loop binding effects, they are consistent with the

larger value of the proton charge radius when two-loop binding effects are included in the QED calculations. Mostly recently, a QED calculation with three-loop binding effects has been carried out ¹². Before accurate comparisons between theory and experiment can be made, either in QCD or QED, a new, high precision experiment on the proton charge radius is urgently needed.

The mean squared charge radius of the neutron is $\langle r_n^2 \rangle = -0.113 \pm 0.003 \pm 0.004$ fm², obtained most recently from an experiment carried out at the Oak Ridge National Laboratory ¹³ in which the neutron transmission through a thorogenic liquid ²⁰⁸Pb has been measured in the neutron energy range between 0.1 and 360 eV.

Among the four nucleon electromagnetic form factors, the neutron electric form factor, G_E^n is of particular interest, but it is also least known due to the lack of free neutron targets and the smallness of G_E^n in general. Its interpretation within many models has been obscured by relativistic effects. Recently, Isgur ¹⁴ demonstrated to leading order in the relativistic expansion of a constituent quark model that the naive interpretation of G_E^n as arising from the neutron's rest frame charge distribution holds due to a cancellation of the Foldy term against a contribution to the Dirac form factor, F_1 . Enormous experimental progress has been made on the nucleon electromagnetic form factors in the last decade or so. In particular, new data with significantly improved precision from double-polarization experiments are available due to the recent advances in polarized target, beam and recoil polarimeter technologies. More precise data from the next generation of double-polarization experiments are anticipated in the next several years, and these data will allow more stringent tests of theoretical descriptions of the nucleon electromagnetic structure. In the next two sections, the experimental progress on the nucleon electromagnetic form factors will be reviewed, in particular the most recent measurements from double-polarization experiments.

3. Unpolarized Electron Scattering and Nucleon Electromagnetic Form Factors

3.1. Elastic Electron-Proton Scattering

In terms of G_E and G_M , the differential cross-section for electron-nucleon scattering can be written in the one-photon-exchange picture as:

$$\frac{d\sigma}{d\Omega_{lab}} = \frac{\alpha^2}{4E^2 \sin^4 \frac{\theta}{2}} \frac{E'}{E} \left(\frac{G_E^2 + \tau G_M^2}{1 + \tau} \cos^2 \frac{\theta}{2} + 2\tau G_M^2 \sin^2 \frac{\theta}{2} \right), \quad (9)$$

where E' and θ are the scattered electron energy and angle, respectively; α is the fine structure constant, and $\tau = \frac{Q^2}{4M^2}$.

The proton electric (G_E^p) and magnetic (G_M^p) form factors have been studied extensively in the past from unpolarized electron-proton (ep) elastic scattering using the Rosenbluth separation technique ¹⁵. Eqn. 9 can be re-written as:

$$\begin{aligned}\frac{d\sigma}{d\Omega} &= \frac{\alpha^2 E' \cos^2 \frac{\theta}{2}}{4E^3 \sin^4 \frac{\theta}{2}} \left[G_E^{p\ 2} + \frac{\tau}{\epsilon} G_M^{p\ 2} \right] \left(\frac{1}{1+\tau} \right) \\ &= \sigma_M \left[G_E^{p\ 2} + \frac{\tau}{\epsilon} G_M^{p\ 2} \right] \left(\frac{1}{1+\tau} \right),\end{aligned}\quad (10)$$

where $\epsilon = (1 + 2(1 + \tau) \tan^2 \frac{\theta}{2})^{-1}$ is the virtual photon longitudinal polarization, and σ_M is the Mott cross section describing the scattering from a pointlike target:

$$\sigma_M = \frac{\alpha^2 E' \cos^2 \frac{\theta}{2}}{4E^3 \sin^4 \frac{\theta}{2}}. \quad (11)$$

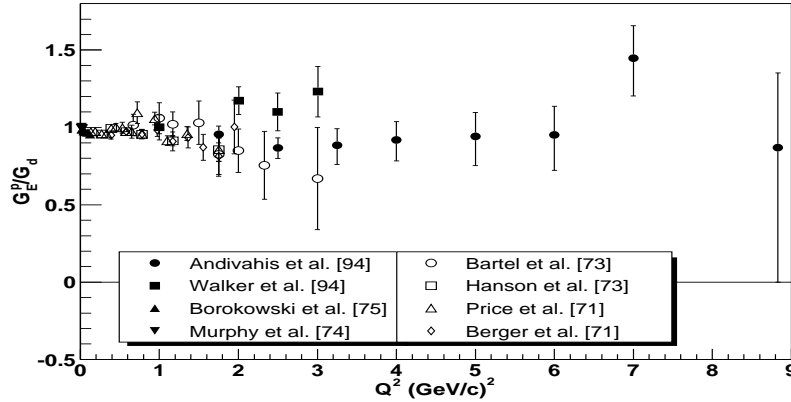


Fig. 2. World data published since 1970 on the proton electric form factor obtained by the Rosenbluth method from the unpolarized cross-section measurements. The data are plotted as $\frac{G_E^p}{G_D}$, where G_D is the standard dipole parameterization.

In the Rosenbluth method, the separation of $G_E^{p\ 2}$ and $G_M^{p\ 2}$ is achieved by measuring the cross section at a given Q^2 value by varying the incident electron beam energy and the electron scattering angle. The measured differential cross section is then plotted as a function of $\tan^2 \frac{\theta}{2}$, and one can extract information on $G_E^{p\ 2}$ and $G_M^{p\ 2}$ from the slope and the intercept of the plotted curve. While the $G_E^{p\ 2}$ term dominates the cross section in the low Q^2 region, the $G_M^{p\ 2}$ term dominates at large Q^2 values. Thus, the extraction of G_M^p at low Q^2 , and G_E^p at large Q^2 values becomes difficult using the Rosenbluth technique. Fig. 2 and Fig. 3 show the world data since 1970¹⁶ on the proton electric and magnetic form

factors, as a function of Q^2 using the Rosenbluth separation technique. The data are shown as $\frac{G_E^p}{G_D}$, and $\frac{G_M^p}{\mu_p G_D}$, respectively, where μ_p is the proton magnetic moment, and $G_D = (1 + Q^2/0.71)^{-2}$ is the standard dipole parameterization, and Q^2 is in $(\text{GeV}/c)^2$.

3.2. Electron-Deuteron Scattering

Because of the lack of free neutron targets, little is known about the neutron electromagnetic structure. The best known quantity is the neutron rms charge radius which is obtained from thermal neutron scattering experiments. The neutron electromagnetic form factors are known with much less precision than the proton electric and magnetic form factors. They have been deduced in the past from elastic or quasielastic electron-deuteron scattering. This procedure involves considerable model dependence. Another complication arises from the fact that the net charge of the neutron is zero. As such the neutron electric form factor G_E^n is much smaller than its magnetic form factor G_M^n . Therefore, the magnetic part of the contribution dominates the cross section, which makes it very difficult to extract G_E^n from unpolarized cross section measurements using deuterium targets.

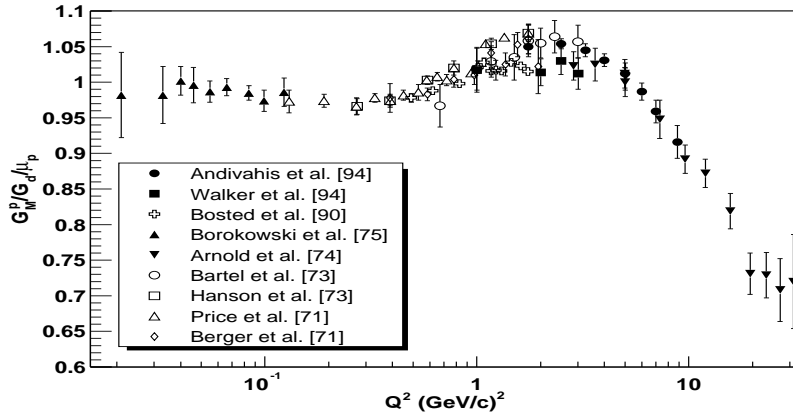


Fig. 3. World data published since 1970 on the proton magnetic form factor obtained using the Rosenbluth method from unpolarized cross-section measurements. The data are plotted as $\frac{G_M^p}{\mu_p G_D}$, in the unit of the standard dipole parameterization.

3.2.1. The Elastic Electron-Deuteron Scattering

The cross section for the unpolarized elastic electron-deuteron scattering in the

one-photon-exchange approximation is described by the Rosenbluth formula,

$$\frac{d\sigma}{d\Omega} = \sigma_M \left[A(Q^2) + B(Q^2) \tan^2 \frac{\theta}{2} \right]. \quad (12)$$

The two structure functions: $A(Q^2)$ and $B(Q^2)$ can be separated by the Rosenbluth separation technique discussed previously. The deuteron is a spin-1 nucleus and the characterization of its charge and magnetization distribution requires three form factors: $F_C(Q^2)$, $F_Q(Q^2)$, $F_M(Q^2)$, the charge monopole, quadrupole and the magnetic dipole form factor, respectively. The structure functions $A(Q^2)$ and $B(Q^2)$ can be expressed in terms of these three form factors as

$$A(Q^2) = F_C^2(Q^2) + \frac{8}{9}\tau^2 F_Q^2(Q^2) + \frac{2}{3}\tau F_M^2(Q^2), \quad (13)$$

$$B(Q^2) = \frac{4}{3}\tau(1 + \tau)F_M^2(Q^2), \quad (14)$$

where $\tau = \frac{Q^2}{4M_d^2}$. Thus, it is not possible to separate all three form factors of the deuteron from the unpolarized elastic electron-deuteron cross section measurement alone. An additional measurement which involves polarization is necessary to separate the charge monopole and the charge quadrupole form factors. Such a polarization experiment can be either a deuteron tensor polarization measurement employing a polarimeter by using an unpolarized electron beam and an unpolarized deuteron target or an analyzing power measurement by using a polarized deuteron target and an unpolarized electron beam.

The tensor moment t_{20} is particularly interesting due to its sensitivity to F_C . It is defined as

$$t_{20} = \left(\frac{1}{\sqrt{2}} \right) \langle 3S_z^2 - 2 \rangle = \frac{1}{\sqrt{2}} \left[\frac{N_+ + N_- - 2N_0}{N_+ + N_- + N_0} \right], \quad (15)$$

where N_+ , N_- , and N_0 are the occupation numbers for the deuteron magnetic substate $M_s = 1, 0, -1$, respectively. The deuteron tensor moment t_{20} can be expressed in terms of the deuteron form factors as:

$$t_{20} = \frac{-1}{\sqrt{2}I_0} \left[\frac{8}{3}\tau F_C F_Q + \frac{8}{9}\tau^2 F_Q^2 + \frac{1}{3}\tau(1 + 2(1 + \tau) \tan^2 \frac{\theta}{2}) F_M^2 \right], \quad (16)$$

where $I_0 = A(Q^2) + B(Q^2) \tan^2 \frac{\theta}{2}$. Therefore, by combining the structure functions $A(Q^2)$, $B(Q^2)$ from the unpolarized cross section measurement, and the deuteron tensor moment t_{20} measurement, one can separate all three deuteron form factors.

The structure function $A(Q^2)$ provides one of the few methods to infer the neutron electric form factor, especially in the low Q^2 region (less than 1.0 (GeV/c)²) where theoretical descriptions of $A(Q^2)$ including relativity, meson-exchange currents (MEC), etc. are under better control compared to higher Q^2 region. The most systematic information on G_E^n at low Q^2 , prior to any polarization experiment, is

from the $A(Q^2)$ structure function determined from the elastic electron-deuteron scattering experiment by Platchkov *et al.* ¹⁷. However, the extraction procedure is quite complicated. First, the subtraction of $F_M^2(Q^2)$ from $A(Q^2)$ using data on $B(Q^2)$ is performed to obtain the corrected $A(Q^2)$ which contains contributions from $F_C(Q^2)$, and $F_Q(Q^2)$ only. Second, the relativistic and MEC corrections are applied to the corrected $A(Q^2)$ to obtain the corresponding $A(Q^2)$ in the impulse picture. Next, the deuteron structure is removed to obtain the nucleon iso-scalar charge form factor. Finally, the proton electric form factor is subtracted from the nucleon iso-scalar charge form factor and G_E^n is obtained. The extracted G_E^n values are extremely sensitive to the deuteron structure. Fig. 4 shows the G_E^n values extracted with the Paris nucleon-nucleon potential ¹⁸ together with a fit of the data (dash-dotted curve). Results from fitting the G_E^n data extracted with the Nijmegen potential ¹⁹, the Argonne V14 (AV14) ²⁰ and the Reid-Soft Core (RSC) ²¹ NN potentials are shown as solid, dashed and dotted curves, respectively. The large spread represents the uncertainty of G_E^n due to the deuteron structure, and the absolute scale of G_E^n contains a systematic uncertainty of about 50% from such an extraction.

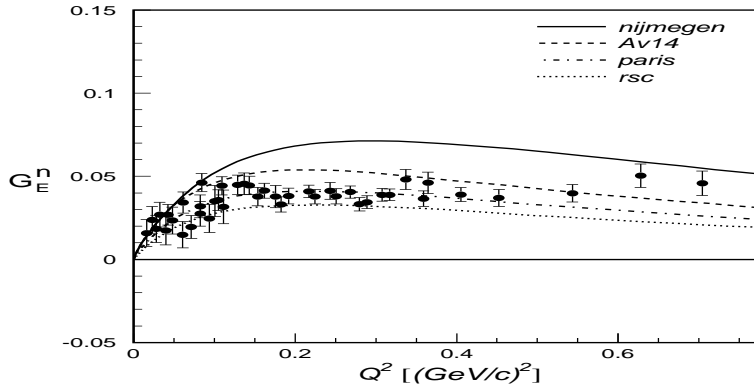


Fig. 4. The electric form factor of the neutron, G_E^n , as a function of four-momentum transfer squared from the unpolarized electron-deuteron elastic scattering measurement by Platchkov *et al.* ¹⁷.

Recently, Schivilla and Sick ²² extracted G_E^n from an analysis of the deuteron quadrupole form factor $F_Q(Q^2)$ data. Such an approach is different from the anal-

ysis employing the structure function $A(Q^2)$ discussed above, in which both the charge monopole and quadrupole deuteron form factors contribute. State-of-the-art deuteron calculations based on a variety of different model interactions and currents show that the F_Q form factor is relatively insensitive to the uncertain two-body operators of shorter range because the long-range one-pion exchange operator dominates the two-body contribution to F_Q . Also, data on the F_Q form factor has improved tremendously with the measurements of the polarization observable t_{20} in electron-deuteron elastic scattering. As such, the neutron electric form factor has been extracted up to a Q^2 value above 40 fm^{-2} (1.55 (GeV/c)^2) from $F_Q(Q^2)$ without undue systematic uncertainties from theory. These extracted values of G_E^n will be presented later together with G_E^n data from double-polarization experiments.

3.2.2. Quasielastic Electron-Deuteron Scattering

Quasielastic electron-deuteron scattering, in which the kinematics of the electron scattering from the nucleon inside the deuteron is selected, is the other process involving the deuteron which has been used extensively in probing the electromagnetic structure of the neutron. It includes both inclusive measurements, in which only scattered electrons are detected at the quasielastic kinematics, and coincidence measurements where both the scattered electron and the knockout neutron are measured.

The missing mass squared for quasielastic $e - d$ scattering is defined as, $W^2 = M^2 + 2M(E - E') - Q^2$, where M is the nucleon mass; $W^2 = M^2 = 0.88 \text{ GeV}^2$ at the quasielastic peak. The measured quasielastic $e - d$ cross-section per nucleon, $\sigma(E, E', \theta)$ converted to the reduced cross section is written as:

$$\sigma_R = \epsilon(1 + \tau') \frac{\sigma(E, E', \theta)}{\sigma_M} = R_T + \epsilon R_L, \quad (17)$$

where σ_M is the Mott cross section defined earlier, and R_T and R_L are the transverse and longitudinal nuclear response functions, respectively. In the plane wave impulse approximation (PWIA) the quasielastic R_T response function is proportional to $G_M^n^2 + G_M^p^2$, and the R_L response function is proportional to $G_E^n^2 + G_E^p^2$. Thus, the extraction of the neutron electromagnetic form factor requires the separation of the R_L and the R_T response functions using the Rosenbluth technique, followed by the subtraction of the proton contribution in PWIA.

Until recently, most data on G_M^n had been deduced from quasi-elastic electron-deuteron scattering. For inclusive measurements^{23,24,25,26,27}, the procedure requires the separation of the longitudinal and transverse cross sections and the subsequent subtraction of a large proton contribution. Thus, it suffers from large theoretical uncertainties due in part to the deuteron model employed and in part to corrections for final-state interactions (FSI), MEC effects, and relativistic corrections. The proton subtraction can be avoided by measuring the neutron in coincidence $d(e, e'n)$, but the difficulty is associated with the absolute neutron detection efficiency calibration. This method was used by Stein *et al.*²⁸, Bartel *et al.*²⁹, and most recently

at MIT-Bates Laboratory by Markowitz *et al.* ³⁰. In addition, the anti-coincident $d(e, e'\bar{p})$ measurement, where the absence of the proton detection is required, was also carried out in the past ^{31,32}.

The sensitivity to nuclear structure can be greatly reduced by taking the cross-section ratio of $d(e, e'n)$ to $d(e, e'p)$ at quasi-elastic kinematics. Several recent experiments ^{33,34,35,36} have employed this technique to extract G_M^n with uncertainties of $<2\%$ ^{35,36} for Q^2 -values from 0.1 to 0.8 (GeV/c)². While such level of precision is excellent, there is considerable disagreement among the results ^{30,33,34,35,36} concerning the absolute value of G_M^n . All coincidence experiments require an absolute calibration of the neutron detection efficiency, which is a challenging task. Most recently, the G_M^n measurement using the ratio technique has been extended to a Q^2 value of above 4.0 (GeV/c)² at Jefferson Lab ³⁷. While discrepancies among the deuterium experiments described above may be understood ³⁸, additional data on G_M^n , preferably obtained using a complementary method, are highly desirable. The inclusive quasi-elastic reaction ${}^3\text{He}(\vec{e}, e')$ provides just such an alternative approach. In comparison to deuterium experiments, this technique employs a different target and relies on polarization degrees of freedom, and is therefore subject to completely different systematics. We will discuss this type of double-polarization measurements in the next section. The world data on G_M^n from unpolarized ed quasielastic scattering experiments are shown in Fig. 5.

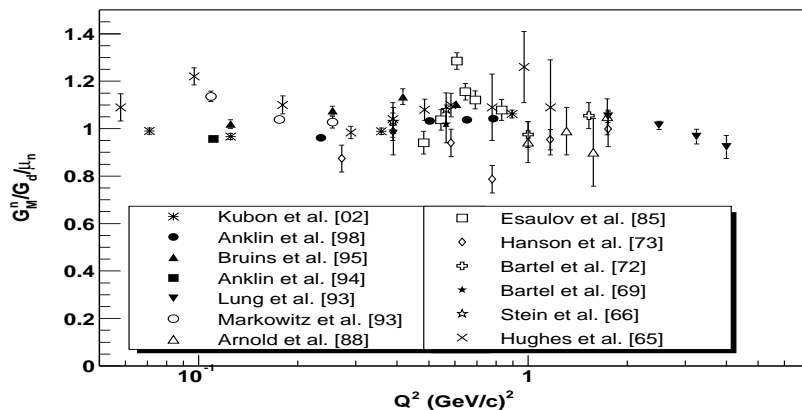


Fig. 5. The published neutron magnetic form factor data from unpolarized deuterium experiments [23-36]. The data are plotted as G_M^n/μ_n , in units of the standard dipole form factor G_D , as a function of Q^2 .

4. Double-Polarization Electron Scattering Experiments

Polarization degrees of freedom in electron scattering have proven to be very useful in extracting information about small amplitude processes by isolating terms sensitive to the interference of the small amplitude with a much larger amplitude. The ability to selectively isolate certain combinations of amplitudes that either polarized electron beams or polarized targets (recoil polarimeters) have historically provided when used in isolation, is significantly enhanced by using them together. Thus, polarized electron scattering from polarized targets, and polarization transfer measurements using recoil polarimeters can provide important information on the nucleon spin structure and the electromagnetic structure of the nucleon.

The development of polarized beams, polarized targets and recoil polarimeters has allowed more complete studies of electromagnetic structure than has been possible with unpolarized reactions. In quasielastic scattering, the spin degrees of freedom introduce new response functions into the differential cross section, which provides additional information on nuclear structure³⁹. Such studies are especially important for probing the neutron electromagnetic structure because of the lack of free neutron targets in nature. Section 4.1 contains a brief overview of experimental techniques employed in double polarization experiments.

4.1. *Experimental Techniques in Double-Polarization Experiments*

4.1.1. Polarized electron beam

Polarized electrons can be produced by various techniques⁴⁰. Photoemission from GaAs has several advantages: high peak current, helicity reversal by optical means, and the feasibility of building a GaAs source with small transverse phase space or emittance, an important requirement for some electron accelerator machines.

The GaAs polarized electron source works through photo-emission of electrons that have been polarized through optical pumping. The electron beam is generated by illuminating a GaAs cathode, which is placed in ultra-high vacuum, with high-intensity circularly polarized laser light. Strained GaAs cathodes are frequently used nowadays and have advantage over conventional bulk GaAs cathodes. The strain creates a gap in the different sub-levels of the $P_{3/2}$ electrons in the valence bands of the GaAs⁴¹. Left circularly polarized light with the right frequency, incident on the GaAs, only drives transition between the $P_{3/2}$ $m=3/2$ state in the valence band and the $S_{1/2}$ $m=1/2$ level of the conduction band. From there the polarized electrons diffuse to the surface and escape into the surrounding vacuum. Typically, the surface of the GaAs cathode is treated with cesium to create a negative electron affinity. The polarization of source electrons is consequently as high as 80%.

The electrons from the polarized source are longitudinally polarized, and are then accelerated in the linac. The electron beam polarization can be determined either by using a Møller polarimeter which measures the asymmetry from polarized electrons scattering off polarized atomic electrons in a magnetized iron foil, or by

using a Compton polarimeter in which the asymmetry from circularly polarized laser light backscattering from the polarized electron beam is measured. In some of the high precision asymmetry measurements, both polarimeters might be employed to minimize systematic uncertainties in the determination of the electron beam polarization.

4.1.2. Polarized targets

Polarized targets for studies of nucleon structure can be categorized as polarized proton targets and polarized effective neutron targets because of the lack of free, stable neutrons in nature. For the purpose of a brief overview of polarized targets, the discussion below is organized according to gaseous and solid targets.

There are two general types of polarized gaseous targets: external and internal. External targets are sealed targets with windows. They are much more dense than internal targets in order to achieve a practical luminosity with relatively low incident electron beam currents. The windowless internal targets placed in an electron storage ring with very high electron beam currents are open flowing systems, thus with much thinner average target thicknesses compared to external targets.

The internal gas targets are typically polarized by either optical pumping or by the atomic beam source method. Optical pumping is widely used to polarize a sample of atoms by transferring angular momentum from a pump light beam, typically a laser beam, to the sample atoms. The atomic beam source (ABS) method is based on the well-known principle of Stern-Gerlach separation and radio frequency (RF) transitions. One can employ either the atomic beam source method which is a well-established technique, or the optical pumping method for polarized hydrogen (proton) and deuterium (effective neutron) internal targets. The typical atomic flux an ABS can feed a storage target cell is $\sim 6 \times 10^{16}$ atoms/second and the proton and deuteron nuclear vector polarization can be as high as 90%.

An internal polarized H/D gas target is also feasible with spin-exchange optical pumping method. Such a target works in the following way: polarized laser light optically pumps alkali atoms. Hydrogen (deuterium) atoms are polarized through spin-exchange collisions with the alkali atoms. At large hydrogen (deuterium) densities, frequent H-H (D-D) collisions enhance the probability of hyperfine interactions, and the system approaches spin temperature equilibrium⁴². The nucleus is polarized in spin temperature equilibrium, in which hydrogen nuclear and atomic polarizations are the same and, in the case of deuterium nuclear vector polarization exceeds the atomic polarization. Spin-exchange optical pumping of alkali-metal atoms with hydrogen (deuterium) is an efficient way to polarize hydrogen (deuterium) atoms and atomic fluxes as high as 10^{18} atoms/second are typical with this type of source, though with much lower nuclear polarization than that of ABS, a 50% nuclear vector polarization for hydrogen and 60% for deuterium can be anticipated.

Polarized ^3He is useful for studying the neutron structure because its ground state is dominated by a spatially symmetric S wave in which the proton spins cancel

and the spin of the ^3He nucleus is predominantly carried by the unpaired neutron alone. Internal polarized ^3He gas targets can be produced in principle either by using optical pumping methods or atomic beam source method. However, only metastability-exchange optical pumping has been used up to now in producing internal targets of practical thicknesses for scattering experiments. In the case of ^3He , direct optical pumping between its ground state and the first excited state is not possible because of the energy difference involved. The metastability-exchange optical pumping involves optical pumping of 2^3S_1 metastable state atoms, then transferring the polarization to ^3He ground state atoms through metastability-exchange collisions.

The only external gaseous targets that exist for scattering experiments are polarized ^3He targets based on both the metastability-exchange optical pumping technique and the spin-exchange optical pumping technique in which rubidium vapor is typically used as the spin-exchange medium. While spin-exchange optical pumping is capable of producing high density targets, metastability-exchange optical pumping combined with mechanical compression produce polarized ^3He targets of comparable densities. External polarized ^3He targets based on these techniques have been used successfully at electron accelerator laboratories around the world. For more details about these gaseous polarized targets, we refer the reader to a review article by Chupp, Holt and Milner ⁴³.

Polarized solid targets have been used widely in lepton scattering experiments probing nucleon structure, particularly in deep-in-elastic lepton scattering experiments studying nucleon spin structure. The SMC experiment ⁴⁴ at CERN used a low intensity muon beam incident on a very thick target of butanol or deuterated butanol, which was cooled by a powerful dilution refrigerator. Polarization is achieved by the technique of dynamic nuclear polarization, which works in the following way. A hydrogeneous compound is doped with a small concentration (10^{-4}) of unsaturated electron spins. In a large magnetic field and low temperatures these electrons are polarized from the Boltzmann distribution. At a temperature of 1 K and a magnetic field of 5 Tesla, the electron polarization is 99.8%. The relaxation time of the electrons in the higher-energy state is short ($\sim 10^{-3}$ second) due to the interaction of the electrons with the lattice. The electrons therefore flip back and are available for further spin-flip transitions with other protons (deuterons). The relaxation time of the nuclei, on the other hand, is long ($\sim 10^3$ second). This allows the nuclei to accumulate preferentially in a state selected by the frequency of the microwaves, thus leading to a high polarization of the sample. Experiments at SLAC (E143, E155) ^{45,46} and Jefferson Lab used polarized solid NH_3 and ND_3 targets ^{47,48} based on the same technique of dynamic nuclear polarization. We refer interested readers to Ref. ⁴⁹ for details on these targets.

4.1.3. *Recoil polarimeters*

Focal plane polarimeters were standard equipment at intermediate energy proton accelerators, such as LAMPF ⁵⁰, TRIUMF ⁵¹, SATURNE ⁵², and PSI ⁵³. Sensi-

tivities of spin observables to small amplitudes were demonstrated by experiments carried out at these facilities using focal plane polarimeters. In recent years, proton recoil polarimeters have been employed in a number of experiments at electron accelerator facilities, such as the MIT-Bates Laboratory ⁵⁴, the Mainz laboratory ⁵⁵ and the Jefferson Laboratory ^{56,57,58}.

Proton polarimeters are based on nuclear scattering from an analyzer material like carbon. The proton-nucleus spin-orbit interaction results in an azimuthal asymmetry in the scattering distribution which can be analyzed to obtain the proton polarization and spin orientation. A typical proton recoil polarimeter consists of two front detectors to track incident protons, followed by a carbon analyzer and two rear detectors to track scattered particles. Recoil neutron polarimeters which have been used in experiments to extract neutron electric form factor are based on the same physics principle and are constructed in similar ways.

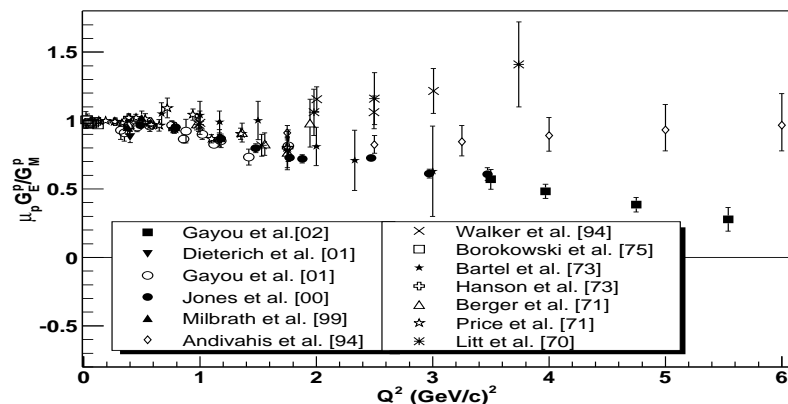


Fig. 6. World data on the proton electric and magnetic form factor ratio, $\frac{\mu_p G_E^p}{G_M^p}$, as a function of Q^2 . The high precision data from polarization transfer measurements at Jefferson Lab by Gayou et al. ⁵⁸ and by Jones et al. ⁵⁶ plotted with statistical uncertainties only, show different Q^2 -dependence of the form factor ratio from those obtained by the Rosenbluth method from unpolarized cross-section measurements, at large values of Q^2 .

4.2. Polarized Electron-Proton Elastic Scattering

While precise information on G_E^p and G_M^p is important for understanding the underlying electromagnetic structure of the proton, it is also very interesting to study the ratio of these two form factors, $\frac{\mu_p G_E^p}{G_M^p}$ as a function of Q^2 . Any Q^2 dependence in the proton form factor ratio would suggest different charge and magnetization spa-

tial distributions inside the proton. Double polarization experiments allow precise measurement of the proton form factor ratio directly. Furthermore, by combining polarization measurements with differential cross-section measurements, one can determine G_E^p and G_M^p separately with significantly improved precision compared to the conventional Rosenbluth separation technique.

In the one-photon-exchange Born approximation, the elastic scattering of longitudinally polarized electrons from unpolarized protons results in a transfer of polarization to the recoil proton with only two nonzero components: P_t perpendicular to, and P_l parallel to the proton momentum in the scattering plane⁵⁹. The form factor ratio can be determined from a simultaneous measurement of the two recoil polarization components in the scattering plane:

$$\frac{G_E^p}{G_M^p} = -\frac{P_t}{P_l} \frac{E + E'}{2M} \tan\left(\frac{\theta}{2}\right), \quad (18)$$

where E and E' are the incident and scattered electron energy, respectively, and θ is the electron scattering angle.

Although no dramatic Q^2 -dependence in the proton form factor ratio has been observed from unpolarized measurements, new data from a polarization transfer experiment⁵⁶, which measured this ratio directly shows very intriguing behavior at higher Q^2 , i.e., G_E^p falls off much faster than G_M^p as a function of Q^2 . The intriguing result on $\frac{\mu_p G_E^p}{G_M^p}$ at high Q^2 values from Jefferson Lab⁵⁶ has motivated much interest on this subject both experimentally⁵⁷ and theoretically. A more recent polarization transfer experiment at Jefferson Lab⁵⁸ showed that the downward trend continues out to $Q^2 = 5.6$ (GeV/c)². Prior to the Jefferson Lab experiments, the recoil polarization technique was employed at the MIT-Bates laboratory⁵⁴; and it has also been used more recently at Mainz⁵⁵. Fig. 6 shows the world data on the proton form factor ratio with statistical uncertainties only from these recoil polarization measurements, as well as those obtained from unpolarized experiments. The new data from polarization experiments at Jefferson Lab show unprecedented precision compared to the data from unpolarized experiments. These new data demonstrated an intriguing Q^2 dependence, dramatically different from the behavior observed in the unpolarized Rosenbluth separation experiments. Recently, a new experiment was completed at Jefferson Lab⁶⁰ aiming at resolving such a discrepancy by using the so-called super Rosenbluth separation technique. Results from this experiment are anticipated in the near future.

Alternatively, one can determine the proton form factor ratio by measuring the asymmetry of longitudinally polarized electrons scattered from a polarized proton target. The one-photon-exchange diagram for such spin-dependent elastic scattering is shown in Fig. 7. For longitudinally polarized electrons scattering from a polarized proton target, the differential cross section can be written as³⁹:

$$\frac{d\sigma}{d\Omega} = \Sigma + h\Delta, \quad (19)$$

where Σ is the unpolarized differential cross section given by Eqn. 9, h is the electron helicity, and Δ is the spin-dependent differential cross section given by:

$$\Delta = -\sigma_{Mott} f_{recoil}^{-1} [2\tau v_{T'} \cos \theta^* G_M^p{}^2 - 2\sqrt{2\tau(1+\tau)} v_{TL'} \sin \theta^* \cos \phi^* G_M^p G_E^p], \quad (20)$$

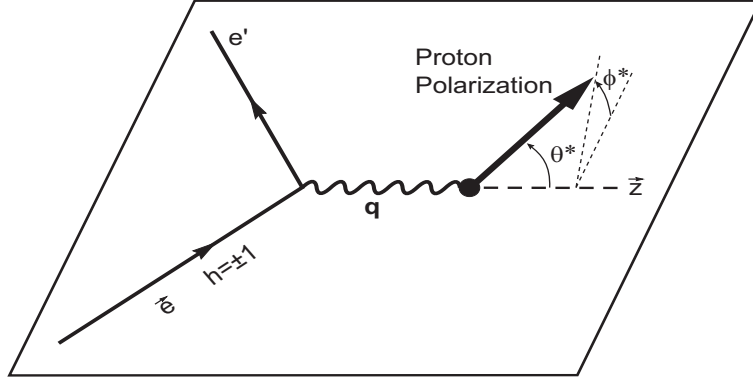


Fig. 7. The one-photon-exchange diagram for spin-dependent electron-nucleon elastic scattering.

where θ^* and ϕ^* are the polar and azimuthal proton spin angles defined with respect to the three-momentum transfer vector \vec{q} and the scattering plane (Fig. 7), and $v_{T'}$ and $v_{TL'}$ are kinematic factors³⁹.

The spin-dependent asymmetry A is defined as:

$$A = \frac{\sigma^{h+} - \sigma^{h-}}{\sigma^{h+} + \sigma^{h-}}, \quad (21)$$

where $\sigma^{h\pm}$ denotes the differential cross section for the two different helicities of the polarized electron beam. The spin-dependent asymmetry A can be written in terms of the polarized and unpolarized differential cross-sections as:

$$A = \frac{\Delta}{\Sigma} = -\frac{2\tau v_{T'} \cos \theta^* G_M^p{}^2 - 2\sqrt{2\tau(1+\tau)} v_{TL'} \sin \theta^* \cos \phi^* G_M^p G_E^p}{(1+\tau) v_L G_E^p{}^2 + 2\tau v_T G_M^p{}^2}. \quad (22)$$

The experimental asymmetry A_{exp} , is related to the spin-dependent asymmetry of Eqn. 22 by the relation

$$A_{exp} = P_b P_t A, \quad (23)$$

where P_b and P_t are the beam and target polarizations, respectively. A determination of the ratio $\frac{G_E^p}{G_M^p}$, independent of the knowledge of the beam and target polarization, can be precisely obtained by forming the so-called super ratio

$$R = \frac{A_1}{A_2} = \frac{2\tau v_{T'} \cos \theta_1^* G_M^p{}^2 - 2\sqrt{2\tau(1+\tau)} v_{TL'} \sin \theta_1^* \cos \phi_1^* G_M^p G_E^p}{2\tau v_{T'} \cos \theta_2^* G_M^p{}^2 - 2\sqrt{2\tau(1+\tau)} v_{TL'} \sin \theta_2^* \cos \phi_2^* G_M^p G_E^p}, \quad (24)$$

where A_1 and A_2 are elastic electron-proton scattering asymmetries measured at the same Q^2 value, but two different proton spin orientations corresponding to (θ_1^*, ϕ_1^*) and (θ_2^*, ϕ_2^*) , respectively. For a detector configuration that is symmetric with respect to the incident electron momentum direction, A_1 and A_2 can be measured simultaneously by forming two independent asymmetries with respect to either the electron beam helicity or the target spin orientation in the beam-left and beam-right sector of the detector system, respectively. Thus, the proton form factor ratio can be determined with high precision using this technique, and an experiment is currently planned at the MIT-Bates Laboratory⁶¹. Such an experiment is essential because it employs a different experimental technique that has different systematic uncertainties than those from recoil proton polarization experiments, and those from Rosenbluth and super Rosenbluth measurements.

4.3. Polarized Quasielastic Electron-Nucleus Scattering and Neutron Electromagnetic Form Factors

4.3.1. Experiments with Deuterium Targets

Measurements of the neutron electric form factor are extremely challenging because of the lack of free neutron targets, the smallness of the G_E^n , and the dominance of the magnetic contribution to the unpolarized differential cross-section. A promising approach to measure G_E^n is by using polarization degrees of freedom. For coincidence elastic scattering of longitudinally polarized electrons from “free” neutrons, $n(\vec{e}, e'\vec{n})$ process, the recoil neutron polarization is given by⁵⁹:

$$P_z = \frac{hP_e}{\epsilon G_E^{n2} + \tau G_M^{n2}} \frac{E + E'}{M} \epsilon \sqrt{\tau(1 + \tau)} G_M^{n2} \tan^2\left(\frac{1}{2}\theta\right) \quad (25)$$

$$P_x = \frac{hP_e}{\epsilon G_E^{n2} + \tau G_M^{n2}} (-2\epsilon \sqrt{\tau(1 + \tau)} G_E^n G_M^n) \tan\left(\frac{1}{2}\theta\right), \quad (26)$$

where P_z and P_x are the recoil neutron polarization component along the recoil neutron momentum direction, and transverse to it, respectively, in the scattering plane. Here P_e denotes the absolute value of the electron polarization and $h = \pm 1$ denotes the electron helicity. In the case of a “free” neutron target, the normal component P_y is zero due to time and parity invariance. However, P_y is typically not zero because an effective neutron (nuclear) target must be employed and final state interactions play a role. Thus, by forming the ratio of $\frac{P_x}{P_z}$, the unpolarized cross-section as well as the electron polarization cancels out, providing sensitive experimental access to the neutron form factor ratio,

$$\frac{P_x}{P_z} = \frac{-2M}{E + E'} \left[\tan\left(\frac{1}{2}\theta\right) \right]^{-1} \frac{G_E^n}{G_M^n}. \quad (27)$$

Eqn. 27 is only valid in the PWIA picture and corrections need to be applied when effective neutron targets are used. The deuteron is the simplest effective

neutron target and it is also the most effective neutron target for recoil neutron polarization measurements. Correcting for nuclear binding effect, relativity, reaction mechanisms such as FSI and MEC effects is essential in order to extract reliable information on G_E^n from quasielastic $d(\vec{e}, e'\vec{n})$ reaction. Furthermore, precise information on G_M^n is crucial in order to extract G_E^n because it is the ratio $\frac{G_E^n}{G_M^n}$ to first order that is determined from such a recoil neutron polarization measurement. Experiments with longitudinally polarized electron beams and recoil neutron polarimeters have been carried out at MIT-Bates⁶² and Mainz^{63,64} in the relatively low Q^2 region, and G_E^n has been extracted from the $d(\vec{e}, e'\vec{n})$ process, using the state-of-the-art two-body calculations by Arenhövel⁶⁵. Most recently, such an approach has been employed at Jefferson Lab up to a Q^2 value of 1.5 (GeV/c)²⁶⁶.

Alternatively, one can employ a polarized deuteron target to probe the neutron electric form factor by the $\vec{d}(\vec{e}, en)$ reaction. The scattering cross-section for longitudinally polarized electrons from a polarized deuteron target for the $\vec{d}(\vec{e}, en)$ reaction can be written as⁶⁵:

$$S = S_0 \{1 + P_1^d A_d^V + P_2^d A_d^T + h(A_e + P_1^d A_{ed}^V + P_2^d A_{ed}^V)\}, \quad (28)$$

where S_0 is the unpolarized differential cross section, h the polarization of the electrons, and P_1^d (P_2^d) the vector (tensor) polarization of the deuteron. A_e is the beam analyzing power, $A_d^{V/T}$ the vector and tensor analyzing powers, and $A_{ed}^{V/T}$ the vector and tensor spin-correlation parameters. The polarization direction of the deuteron is defined with respect to the three-momentum transfer vector, \vec{q} . The vector spin-correlation parameter A_{ed}^V contains a term representing the interference between the small neutron electric form factor and the dominant neutron magnetic form factor, when the target spin is perpendicular to the \vec{q} vector direction. Thus, the spin-dependent asymmetry (defined with respect to the electron beam helicity) from the $\vec{d}(\vec{e}, en)$ reaction for vector polarized deuteron gives access to the quantity $\frac{G_E^n}{G_M^n}$ to first order when the target spin direction is aligned perpendicular to \vec{q} . Such experiments are extremely challenging since they involve both neutron detection and a vector polarized deuteron target.

Recently, the neutron electric form factor was extracted for the first time⁶⁷ from a $\vec{d}(\vec{e}, e'n)$ measurement in which a vector polarized deuteron target from an atomic beam source was employed. Most recently, a $\vec{d}(\vec{e}, e'n)$ experiment⁴⁸ using a dynamically polarized solid deuterated ammonia target was carried out at Jefferson Lab and G_E^n was extracted at a Q^2 value of 0.5 (GeV/c)². The precision of G_E^n from these polarization experiments is significantly better than those by Platchkov *et al.*¹⁷ from the unpolarized electron-deuteron elastic scattering measurement. Thus, by using polarization degrees of freedom and coincidence detections of scattered electrons and recoil neutrons, the dominant neutron magnetic contribution and the proton contribution to the scattering process are suppressed and more precise information on the neutron electric form factor can be extracted.

4.3.2. Quasielastic ${}^3\vec{H}e(\vec{e}, e')$ and ${}^3\vec{H}e(\vec{e}, e'n)$ Reactions

A polarized ${}^3\text{He}$ nucleus is effective in studying the neutron electromagnetic form factors because of the unique spin structure of the ${}^3\text{He}$ ground state, which is dominated by a spatially symmetric S wave in which the proton spins cancel and the spin of the ${}^3\text{He}$ nucleus is carried by the unpaired neutron^{68,69}. Fig. 8 shows the one-photon exchange diagram for longitudinally polarized electrons scattering off from a polarized ${}^3\text{He}$ nuclear target at the quasielastic kinematics in the PWIA picture. For inclusive measurement, only the scattered electron is detected; for the coincidence ${}^3\vec{H}e(\vec{e}, e'n)$ measurement, both the scattered electron and the knockout neutron are detected.

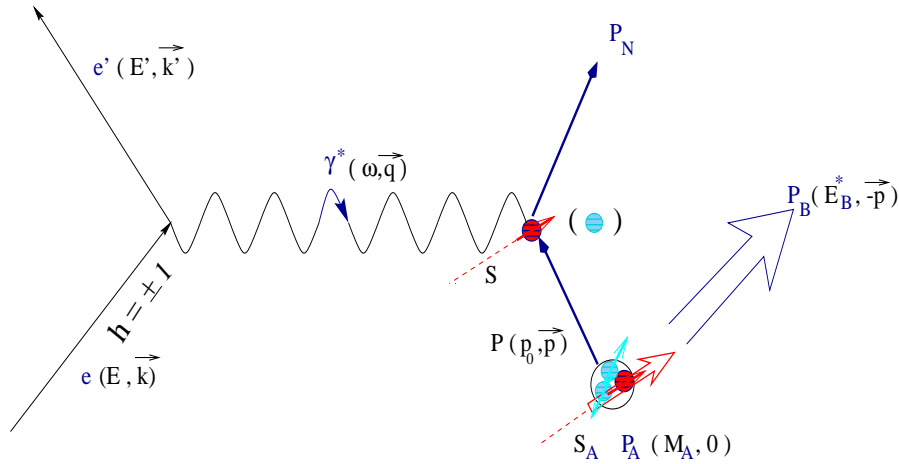


Fig. 8. *The one-photon-exchange diagram for spin-dependent quasielastic electron- ${}^3\text{He}$ scattering in the plane-wave impulse approximation picture.*

The spin-dependent contribution to the inclusive ${}^3\vec{H}e(\vec{e}, e')$ cross section is completely contained in two spin-dependent nuclear response functions, a transverse response $R_{T'}$ and a longitudinal-transverse response $R_{TL'}$ ³⁹. These appear in addition to the spin-independent longitudinal and transverse responses R_L and R_T . These spin-dependent response functions $R_{T'}$ and $R_{TL'}$ can be isolated experimentally by forming the spin-dependent asymmetry A defined previously with respect to the electron beam helicity. In terms of the nuclear response functions, A can be written³⁹:

$$A = \frac{-(\cos \theta^* \nu_{T'} R_{T'} + 2 \sin \theta^* \cos \phi^* \nu_{TL'} R_{TL'})}{\nu_L R_L + \nu_T R_T} \quad (29)$$

where the ν_k are kinematic factors, and θ^* and ϕ^* are the target spin angles defined previously. The response functions R_k depend on Q^2 and the electron energy transfer ω . By choosing $\theta^* = 0$, *i.e.* by orienting the target spin parallel to the momentum transfer \vec{q} , one selects the transverse asymmetry $A_{T'}$ (proportional to $R_{T'}$); by orienting the target spin perpendicular to the momentum transfer \vec{q} ($\theta^* = 90$, $\phi^* = 0$), one selects the transverse-longitudinal asymmetry $A_{TL'}$ (proportional to $R_{TL'}$).

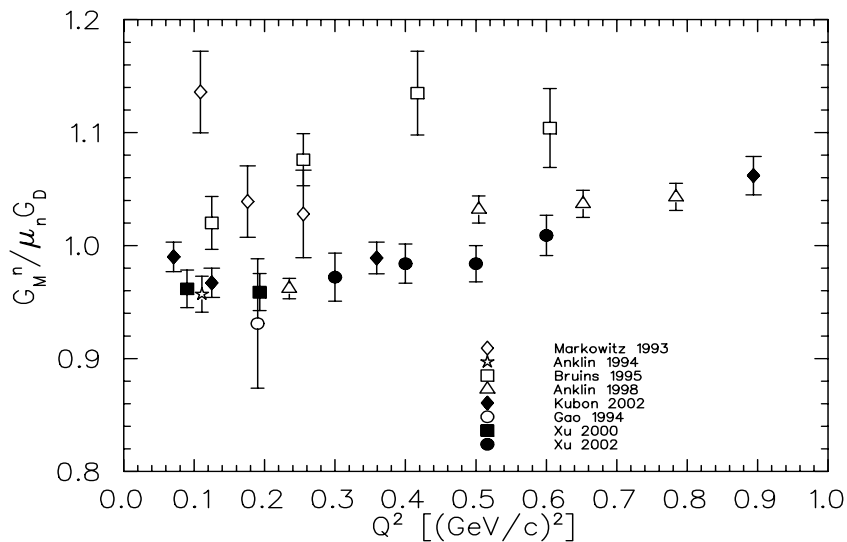


Fig. 9. The neutron magnetic form factor G_M^n data published since 1990, in units of the standard dipole form factor parameterization G_D , as a function of Q^2 . The data by Gao *et al.*⁷⁸, Xu *et al.*^{79,80} are from experiments employing polarized ^3He targets discussed in the text, plotted with statistical uncertainties only. The rest are from experiments involving deuterium targets. The Q^2 points of Anklin 94³³ and Gao 94⁷⁸ have been shifted slightly for clarity.

Because the ^3He nuclear spin is carried mainly by the neutron, $R_{T'}$ at quasi-elastic kinematics contains a dominant neutron contribution and is essentially proportional to $(G_M^n)^2$, similar to elastic scattering from a free neutron. Unlike the free neutron, however, the unpolarized part of the cross section (the denominator in Eq. (29)) contains contributions from both the protons and the neutron in the ^3He nucleus at quasielastic kinematics. Therefore, $A_{T'}$ is expected to first order to have the form $(G_M^n)^2 / (a + b(G_M^n)^2)$ in PWIA, where a is much larger than $b(G_M^n)^2$ in the low Q^2 region. While measurements of G_M^n using deuterium targets enhance the sensitivity to the neutron form factor by detecting the neutron in coincidence, a similar enhancement occurs in inclusive scattering from polarized ^3He because of the cancellation of the proton spins in the ground state. This picture has been confirmed by several PWIA calculations^{70,71,72}, a more recent and more advanced calculation which fully includes FSI⁷³, and most recently by Golak *et al.*⁷⁴, in which both the FSI and MEC effects have been taken into account.

The first experiments^{75,76} which investigated the feasibility of using polarized ^3He targets to study the neutron electromagnetic structure were performed at the MIT-Bates Linear Accelerator Center. Following these two experiments, the first measurement of G_E^n from $^3\text{He}(\vec{e}, e'n)$ was reported by Meyerhoff *et al.*⁷⁷, and the neutron magnetic form factor at low Q^2 was extracted for the first time⁷⁸ from inclusive measurement of the quasielastic transverse asymmetry, $A_{T'}$. Recently, a high precision measurement of $A_{T'}$ ⁷⁹ was carried out in Hall A at Jefferson Lab at six quasielastic kinematic settings corresponding to central Q^2 values of 0.1 to 0.6

(GeV/c)². A state-of-the-art non-relativistic Faddeev calculation ⁷⁴ was employed in the extraction of G_M^n at the two lowest Q^2 values of the experiment and a PWIA calculation ⁷¹ was used in the extraction of G_M^n for the remaining Q^2 values of the experiment ⁸⁰.

The Faddeev calculation treats the ³He target state and the 3N scattering states in the nuclear matrix element in a consistent way by solving the corresponding 3N Faddeev equations ⁸¹. The MEC effects were calculated using the prescription of Riska ⁸², which includes π - and ρ -like exchange terms. The Faddeev based formalism has been applied to other reaction channels and good agreement has been found with experimental results ⁸³, in particular with the recent NIKHEF data on A_y^0 at $Q^2 = 0.16$ (GeV/c)² from the quasielastic ³He($\vec{e}, e'n$) process ⁸⁴, and with the high precision ³He quasielastic asymmetry data in the breakup region ⁸⁵ at low Q^2 from Jefferson Lab. This calculation, while very accurate at low Q^2 , is not expected to be sufficiently precise for a reliable extraction of G_M^n from the ³He asymmetry data in a relatively higher Q^2 region because of its fully non-relativistic nature.

Fig. 9 shows data from the Jefferson Lab experiment ^{79,80}, the earlier MIT-Bates experiment ⁷⁸, and data from deuterium experiments since 1990. The extracted values of G_M^n at Q^2 of 0.1 and 0.2 (GeV/c)² are in good agreement with previous measurements of Anklin *et al.* ^{33,35}. The Jefferson Lab data ⁷⁹ provide the first precision information on G_M^n using a fundamentally different experimental approach than previous deuterium experiments. The extracted G_M^n values ⁸⁰ from the same experiment based on the PWIA calculation ⁷¹ are also shown. While limitations exist in such an approach due to theoretical uncertainties, the results are in very good agreement with the recent deuterium ratio measurements from Mainz ^{35,36}, and in disagreement with results by Bruins *et al.* ³⁴.

Enormous progress has been made in extracting G_M^n from inclusive quasielastic transverse asymmetry $A_{T'}$ measurement in the low Q^2 region due to the new precision data and recent advances in three-body calculations. On the other hand, $A_{TL'}$ from quasielastic ³He(\vec{e}, e') process at low Q^2 ($Q^2 \leq 0.3(\text{GeV}/c)^2$) is dominated by the proton contribution largely because of the smallness of G_E^n and the small non- S wave part of the ³He ground state wave function. Thus, it is unreliable to extract information on G_E^n at low Q^2 from the inclusive ³He(\vec{e}, e') ⁸⁶ process. It is possible to go to higher Q^2 ($Q^2 \geq 0.3(\text{GeV}/c)^2$) to extract G_E^n with respectable accuracy from quasielastic ³He(\vec{e}, e') measurement where the proton contribution to $A_{TL'}$ is under better control. It is more advantageous to determine the neutron electric form factor from the ³He($\vec{e}, e'n$) reaction rather than the ³He(\vec{e}, e') reaction because the proton contribution to the asymmetry is minimized.

The experimental asymmetry for the coincident reaction ³He($\vec{e}, e'n$) at the quasielastic kinematics can be expressed as follows in PWIA:

$$A = -P_e P_n D \frac{2\sqrt{\tau(\tau+1)} \tan(\theta/2) G_E^n G_M^n \sin(\theta^*) \cos(\phi^*)}{G_E^n{}^2 + G_M^n{}^2 (\tau + 2\tau(1 + \tau) \tan^2(\theta/2))} -$$

$$P_e P_n D \frac{2\tau\sqrt{1+\tau+(1+\tau)^2\tan^2(\theta/2)}\tan(\theta/2)G_M^n \cos(\theta^*)}{G_E^n + G_M^n(\tau + 2\tau(1+\tau)\tan^2(\theta/2))} \quad (30)$$

Here P_e is the electron polarization, P_n is the neutron polarization, D is an overall dilution factor which contains dilution from (possible) unpolarized neutrons in the target and dilution from background neutrons generated in (p, n) reactions, e.g. in shielding walls. Eqn. 30 shows the obvious sensitivity to G_E^n in the longitudinal-transverse interference term. Therefore, by aligning the target spin perpendicular to \vec{q} ($A = A_{perp}$), i.e. choosing $\theta^* = 90^\circ$, and $\phi^* = 0^\circ$ the above equation can be rewritten in the following form ($G_E^n \approx 0$):

$$G_E^n = -\frac{A_{perp}}{P_e P_n D} \cdot \frac{G_M^n(\tau + 2\tau(1+\tau)\tan^2(\theta/2))}{2\sqrt{\tau(1+\tau)}\tan(\theta/2)} \quad (31)$$

Aligning the target spin parallel to \vec{q} ($A = A_{long}$) reduces Eqn. 30 to ($G_E^n \approx 0$):

$$A_{long} = -P_e P_n D \frac{2\sqrt{1+\tau+(1+\tau)^2\tan^2(\theta/2)}\tan(\theta/2)}{1+2(1+\tau)\tan^2(\theta/2)}. \quad (32)$$

This equation is completely independent of the neutron form factors and serves as an excellent calibration reaction. Thus, one can combine the above two equations and obtain

$$G_E^n = \sqrt{\tau + \tau(1+\tau)\tan^2(\theta/2)} \frac{A_{perp}}{A_{long}} G_M^n. \quad (33)$$

Precise information on G_M^n is a priori requirement before one can extract G_E^n from such double polarization measurements. The PWIA picture described above is obviously over-simplified. To extract G_E^n reliably, corrections need to be applied, in particular the correction for the FSI effect, which has been carried out recently using the Faddeev approach^{74,87}. There is also technical difficulty involved with detecting knocked out neutrons. Such experiments have been carried out at Mainz and NIKHEF in recent years. The first measurement on G_E^n from ${}^3\text{He}(\vec{e}, e'n)$ was reported by Meyerhoff *et al.*⁷⁷ in which a high pressure polarized ${}^3\text{He}$ target achieved by the metastability-exchange optical pumping technique and the compression method was employed. More recent Mainz measurement by Becker *et al.*⁸⁸ and Rohe *et al.*⁸⁹ using the same technique show much improved statistical accuracy. The FSI correction has been applied⁷⁴ in the extracted G_E^n value from the measurement by Becker *et al.*⁸⁸, which is shown in Fig. 10. While the G_E^n shown in Fig. 10 by Meyerhoff *et al.*⁷⁷ and Rohe *et al.*⁸⁹ do not include corrections for FSI, the FSI effect is expected to be small around a Q^2 value of 0.6 (GeV/c)² and the FSI effect is expected to increase the value of G_E^n by Meyerhoff *et al.*⁷⁷ to a value of around 0.05. Also shown in Fig. 10 are the recent published G_E^n data from double-polarization deuterium experiments discussed previously, the extracted G_E^n values from the deuteron quadrupole form factor data by Schivilla and Sick²², and the Galster parameterization⁹⁰.

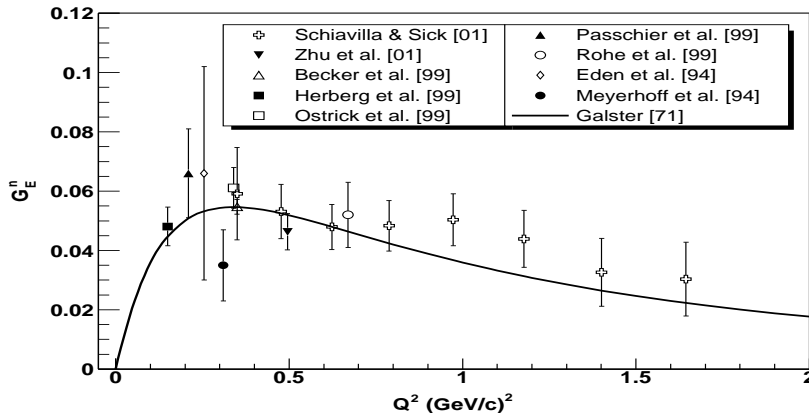


Fig. 10. Recent data on G_E^n from polarization experiments. Also shown are the extracted G_E^n values from the deuteron quadrupole form factor data by Schiavilla and Sick²². The Galster parameterization⁹⁰ is also shown.

Enormous progress has been made in the study of the neutron electromagnetic form factor using polarization degrees of freedom, and in particular with spin-polarized ^3He nuclear targets. However, it is still a very challenging task for both experimenters and theorists. The non-relativistic Faddeev approach has been well tested in the low momentum transfer and low energy transfer regime and reliable information on the neutron electric and magnetic form factor can be extracted in the low Q^2 region. The development of fully relativistic three-body calculations is required to extract the neutron electromagnetic form factors reliably in the relatively higher Q^2 region, which is an extremely difficult task. Recently, Kamada and collaborators⁹¹ solved the relativistic Faddeev equations for the three-nucleon bound state with a Lorentz boosted two-nucleon potential which is introduced in the context of equal time relativistic quantum mechanics. Such a calculation opens the door to considering the relativistic Faddeev equations for three-nucleon scattering.

5. Theoretical Progress

While enormous experimental progress has been made on the subject of nucleon electromagnetic form factors, significant theoretical progress has also been made in recent years in understanding the nucleon electromagnetic structure from the underlying theory of QCD. The newly discovered Generalized Parton Distributions (GPDs)^{92,93}, which can be accessed through deeply virtual Compton scattering and deeply virtual meson production, connect the nucleon form factors and the nucleon structure functions probed in the deep-in-elastic scattering experiments. The GPDs provide new insights into the structure of the nucleon, and provide possibly a complete map of the nucleon wave-function.

QCD is the theory of strong interaction and has been extremely well tested in the high-energy region, i.e., in the perturbative QCD regime. Ideally, one should

calculate the nucleon electromagnetic form factors directly from QCD in the non-perturbative region to confront the data. Unfortunately, nobody knows how to solve QCD analytically in the non-perturbative regime. Lattice QCD calculations based on first principles of QCD, on the other hand, have shown much promise; and this field is evolving rapidly due both to improvements in computer architecture and to new algorithms. While pQCD gives prediction for the nucleon form factors in the perturbative region, QCD effective theories such as the chiral perturbation theory can in principle provide reliable prediction in the very low energy region. In between the low energy region and the pQCD regime, various QCD-inspired models and other phenomenology models exist. Thus, precision data in all experimentally accessible region is crucial in testing these predictions. The rest of the section is devoted to brief discussions of various theoretical approaches used to calculate the nucleon electromagnetic form factors.

5.1. *Scaling and Perturbative QCD*

QCD is an asymptotically free theory, i.e., the strong coupling constant $\alpha_s \rightarrow 0$ as the inter-quark distance $\rightarrow 0$. Thus, one can solve QCD using the perturbation method in the limit of $Q^2 \rightarrow \infty$. Such an approach is the so-called perturbative QCD (pQCD), and specific Q^2 dependence of the nucleon electromagnetic form factors can be obtained from the pQCD analysis.

Brodsky and Farrar⁹⁴ proposed the following scaling law for the proton Dirac (F_1) and Pauli form factor (F_2) at large momentum transfers based on dimensional analysis:

$$F_1 \propto (Q^2)^{-2}, \quad F_2 \sim \frac{F_1}{Q^2}.$$

The helicity-flipping form factor, F_2 , is suppressed by $\frac{1}{Q^2}$ compared to the helicity-conserving form factor F_1 . Such a prediction is a natural consequence of hadron helicity conservation. The hadron helicity conservation arises from the vector coupling nature of the quark-gluon interaction, the quark helicity conservation at high energies, and the neglect of the non-zero quark orbital angular momentum state in the nucleon. In terms of Sach's form factors G_E^p and G_M^p , the scaling result predicts: $\frac{G_E^p}{G_M^p} \rightarrow \text{constant}$ at large Q^2 . Such scaling results were confirmed in a short-distance pQCD analysis carried out by Brodsky and Lepage⁹⁵. Considering the proton magnetic form factor at large Q^2 in the Breit frame, the initial proton is moving in the z direction and is struck by a highly virtual photon carrying a large transverse momentum, $q_\perp^2 = Q^2$. The form factor corresponds to the amplitude that the composite proton absorbs the virtual photon and stays intact. Thus, the form factor becomes the product of the following three probability amplitudes: (i) the amplitude for finding the valence $|qqq\rangle$ state in the incoming proton; (ii) the amplitude for this quark state to scatter from the incoming photon producing the final three-quark state with collinear momenta and (iii) the amplitude for the final three-quark state to reform a proton. The contribution of the proton Fock

states other than the valence $|qqq\rangle$ quark state to the form factor is suppressed as $Q^2 \rightarrow \infty$ because each additional constituent contributes a factor of $\frac{\alpha_s(Q^2)}{Q^2}$ to the amplitude in (ii).

Based on this picture, Brodsky and Lepage obtained the following result within their short-distance pQCD analysis ⁹⁵:

$$\begin{aligned}
 G_M(Q^2) &= \frac{32\pi^2}{9} \frac{\alpha_s^2(Q^2)}{Q^4} \sum_{n,m} b_{nm} \left(\ln \frac{Q^2}{\Lambda^2}\right)^{-\gamma_n-\gamma_m} [1 + O(\alpha_s(Q^2), m^2/Q^2)] \\
 &\rightarrow \frac{32\pi^2}{9} C^2 \frac{\alpha_s^2(Q^2)}{Q^4} \left(\ln \frac{Q^2}{\Lambda^2}\right)^{-4/3\beta} (-e_{\parallel}), \tag{34}
 \end{aligned}$$

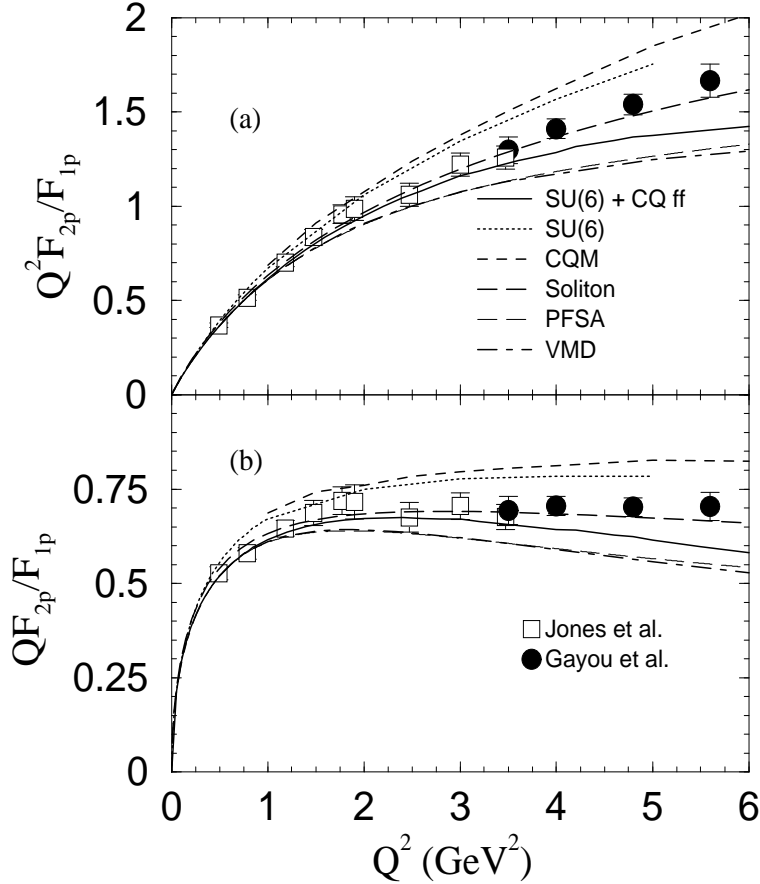


Fig. 11. *The scaled proton Dirac and Pauli form factor ratio: $\frac{Q^2 F_{2p}^p}{F_{1p}^p}$ (upper panel) and $\frac{Q F_{2p}^p}{F_{1p}^p}$ (lower panel) as a function of Q^2 in $(\text{GeV}/c)^2$. The data are from Jones et al. ⁵⁶ and Gayou et al. ⁵⁸ shown with statistical uncertainties only.*

where $\alpha_s(Q^2)$ and Λ are the QCD strong coupling constant and scale parameter, b_{nm} and $\gamma_{m,n}$ are QCD anomalous dimensions and constants, and e_{\parallel} ($-e_{\parallel}$) is the mean total charge of quarks with helicity parallel (anti-parallel) to the nucleon's helicity. For protons and neutrons

$$e_{\parallel}^p = 1, -e_{\parallel}^p = 0, e_{\parallel}^n = -e_{\parallel}^n = -\frac{1}{3},$$

based on the fully symmetric flavor-helicity wave function. While the constants b_{nm} and C are generally unknown for baryons, they are equal for protons and neutrons using isospin symmetry. For the proton electric form factor, one obtains similar result for the Q^2 dependence in the $Q^2 \rightarrow \infty$ limit and as such the short-distance pQCD analysis predicts the same scaling law as the dimensional analysis for the proton form factors: $\frac{G_E^p}{G_M^p} \rightarrow \text{constant}$ and $\frac{Q^2 F_2}{F_1} \rightarrow \text{constant}$. Recently, Belitsky, Ji and Yuan⁹⁶ performed a perturbative QCD analysis of the nucleon's Pauli form factor $F_2(Q^2)$ in the asymptotically large Q^2 limit. They find that the leading contribution to $F_2(Q^2)$ goes like $1/Q^6$, which is consistent with the scaling result obtained by Brodsky and Farrar⁹⁴. The recent Jefferson Lab data^{56,58} on the proton electric and magnetic form factor ratio, $\frac{G_E^p}{G_M^p}$ up to a Q^2 value of 5.5 (GeV/c)^2 show a strong Q^2 dependence in the ratio: the electric form factor falls off much faster than the magnetic form factor. In the naive picture, such Q^2 dependence may suggest that the proton charge is distributed over a larger spatial region than its counterpart, the magnetization. Fig. 11 shows data on the scaled proton Dirac and Pauli form factor ratio $\frac{Q^2 F_2^p}{F_1^p}$ (upper panel) and $\frac{Q F_3^p}{F_1^p}$ (lower panel) from Jefferson Lab experiments^{56,58} as a function of Q^2 together with various predictions. The dash-dotted curve is a new fit based on an improved vector meson dominance model (VMD) by Lomon⁹⁷. The thin long dashed curve is a point-form spectator approximation (PFSA) prediction of the Goldstone boson exchange constituent quark model (CQM)⁹⁸. The solid and the dotted curves are the CQM calculations by Cardarelli and Simula⁹⁹ including SU(6) symmetry breaking with and without constituent quark form factors, respectively. The long dashed curve is a relativistic chiral soliton model calculation¹⁰⁰. The dashed curve is a relativistic CQM calculation by Frank, Jennings, and Miller¹⁰¹.

While the short-distance pQCD analysis⁹⁵ predicts a constant behavior for the $\frac{Q^2 F_2^p}{F_1^p}$ in the $Q^2 \rightarrow \infty$ limit, the data are in better agreement with the $\frac{Q F_3^p}{F_1^p}$ scaling behavior. The data could imply that the asymptotic pQCD scaling region has not been reached or that hadron helicity is not conserved in the experimentally tested regime so far. Such an experimental observation is consistent with studies from polarized deuteron photodisintegration¹⁰², polarized neutral pion production $^1H(\vec{\gamma}, \vec{p})\pi^0$ ¹⁰³, and deuteron tensor polarization measurements $ed \rightarrow e\vec{d}$ ¹⁰⁴. However, Brodsky, Hwang and Hill¹⁰⁵ were able to fit the Jefferson Lab data using a form consistent with pQCD analysis and hadron helicity conservation by taking into account higher twist contributions. Belitsky, Ji and Yuan⁹⁶ also suggest that one should take into account the leading non-vanishing contribution in looking at

the pQCD scaling behavior between F_1^p and F_2^p form factors. On the other hand, Ralston and Jain ¹⁰⁶ argue that the $\frac{QF_2^p}{F_1^p}$ scaling behavior is expected from pQCD when one takes into account contributions to the proton quark wave function from states with non-zero orbital angular momentum.

Following an earlier work by Frank, Jennings and Miller ¹⁰¹, Miller ¹⁰⁷ recently used light front dynamics in modeling the nucleon as a relativistic system of three bound constituent quarks surrounded by a cloud of pions. While the pion cloud is important for understanding the nucleon structure at low momentum transfers, particularly in understanding the neutron electric form factor, quark effects dominate at large momentum transfers. Such a model is able to reproduce the observed constant behavior of $\frac{QF_2}{F_1}$ as a function of Q^2 and the $\frac{QF_2}{F_1}$ ratio is predicted to be a constant up to a Q^2 value of 20 (GeV/c)².

5.2. Lattice QCD Calculations

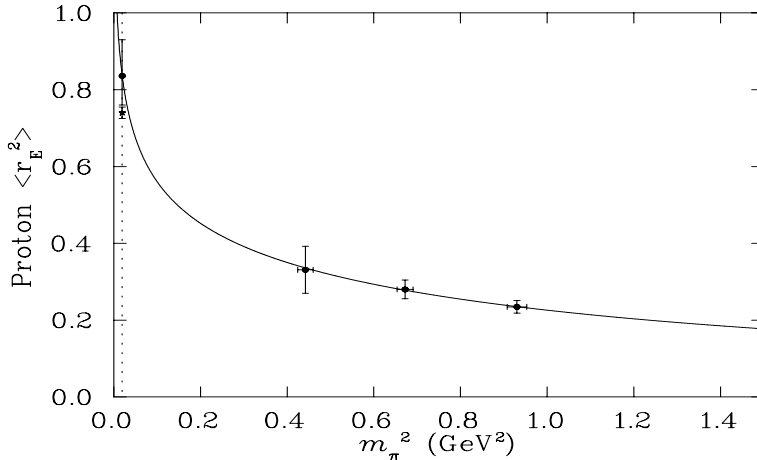


Fig. 12. Fit to the lattice QCD data for the square of the proton charge radius as a function of pion mass squared based on chiral extrapolation ¹¹¹. The extrapolated value at the physical pion mass is shown by the solid dot with the large error bar, and the star indicates the more favorably accepted experimental value ⁶.

The non-perturbative nature of QCD at large distances, i.e. low momentum transfers, prevents the analytical approach in solving QCD. However, important conceptual and technical progress has been made over the years, especially in the last decade or so in solving QCD on the lattice. While full QCD calculations have been carried out in some cases, most of the lattice results obtained so far were carried out in the so-called quenched approximation in which the quark loop contributions, i.e. the sea quark contributions, are suppressed. Furthermore, at present and in the foreseeable future, the lattice calculations are only practical using rather large quark masses because of the limitations of the currently available computational power. As such, uncertainties in extrapolating lattice results to the physical quark mass are rather large, particularly with the naive linear extrapolation in quark

mass. Thus, the challenge is to find an accurate and reliable way of extracting the lattice results to the physical quark mass. The extrapolation methods which incorporate the model independent constraints of chiral symmetry ¹⁰⁸, particularly the leading non-analytic (LNA) behavior of chiral perturbation theory ¹⁰⁹, and the heavy quark limit ¹¹⁰ are exciting recent developments. Recently, such an approach has been used ⁴ in extrapolating the lattice result on the proton root-mean-square (rms) charge radius to the physical pion mass, and at present the extrapolated value is in good agreement with the more favorably accepted experimental value ⁶. Currently, lattice calculations of the nucleon form factor with smaller quark masses are underway ¹¹¹. The anticipated new results together with the improved LNA extrapolation methods will provide more reliable lattice results on the nucleon form factors in the near future.

5.3. Other Calculations of Nucleon Electromagnetic Form Factors

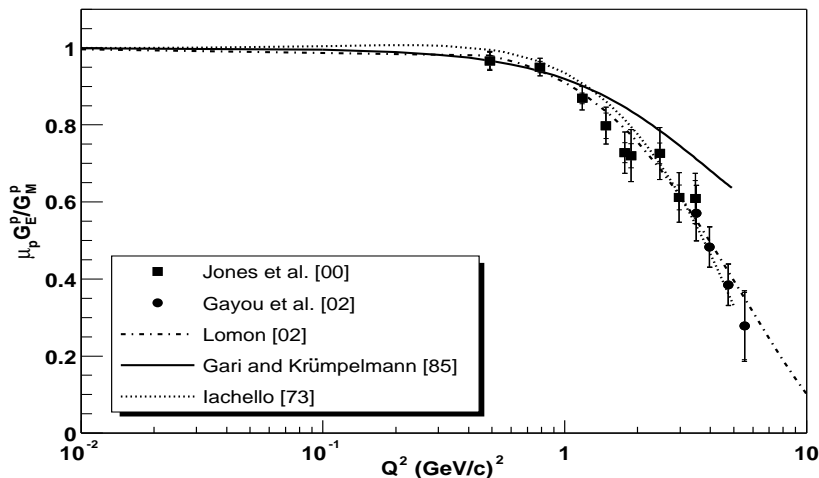


Fig. 13. Jefferson Lab data ^{56,58} on the proton form factor ratio, $\frac{\mu_p G_E^p}{G_M^p}$ as a function of Q^2 together with calculations from various vector meson dominance models ^{112,113,116}.

In this section, we review various models and calculations of the nucleon electromagnetic form factors. While direct comparison between data on proton and neutron electromagnetic form factors and model predictions is important, we will restrict the discussion to those calculations which agree reasonably well with the trend of the recent Jefferson Lab data ^{56,58} on the proton form factor ratio and then look closely to see how well they describe individual form factors. The reason is that the Jefferson Lab data can already eliminate some calculations based on the high Q^2 behavior, thus limiting the number of candidate calculations. In this spirit,

we display the calculations and the Jefferson Lab data versus $\ln(Q^2)$ which, while showing the Jefferson Lab data and the agreement (or lack thereof) of the various models, accentuates the low Q^2 region where lattice QCD and chiral perturbation theory are promising in making reliable predictions.

One of the earlier attempts to describe the proton form factors was a semi-phenomenological fit by Iachello and co-workers¹¹² based on a model in which the scattering amplitude is written as an intrinsic form factor of a bare nucleon multiplied by an amplitude derived from the interaction with the virtual photon via vector meson dominance (VMD). Various forms of the intrinsic bare nucleon form factor were used: dipole, monopole, eikonal. However, since this function is multiplicative, it cancels out in the ratio G_E^p/G_M^p . The VMD amplitude was written in terms of parameters fit to data. Gari and Krümpelmann¹¹³ extended the VMD model to include quark dynamics at large Q^2 via perturbative QCD. Because of the freedom in fitting the parameters, this model was later¹¹⁴ able to describe a subsequent set of data from SLAC that reported the ratio $\mu_p G_E^p/G_M^p$ growing significantly larger than 1 at large values of Q^2 ¹¹⁵. Lomon⁹⁷ extended the Gari and Krümpelmann model¹¹³ by including the width of the ρ meson and the addition of higher mass vector meson exchanges. Such a model has been extended further¹¹⁶ to include the $\omega'(1419)$ isoscalar vector meson pole in order to describe the new Jefferson Lab proton form factor ratio data^{56,58}. Fig. 13 shows the new proton form factor ratio data as a function of Q^2 together with predictions from various VMD models discussed above. While these models have little absolute predictive power, once the high Q^2 data have fixed the parameters, the approach to low Q^2 is highly constrained. One can clearly observe that there is significant difference between these calculations in the low Q^2 domain.

Höhler *et al.*¹¹⁷ fit a dispersion ansatz to $e - N$ scattering data. VMD contributions from ρ , ω , ϕ , ρ' , and ω' were included and parametrized. From these fits to data available at the time, a ratio $\mu_p G_E^p/G_M^p$ is obtained which is in good agreement with the present Jefferson Lab data up to $Q^2 \approx 3 \text{ GeV}^2$, as shown in Fig. 14, at which point the fitted curve begins to rise in contradiction to the trend of the most recent data from Jefferson Lab. In addition, the best fit results in a value for the rms proton radius of 0.84 fm, about 4% lower than the currently accepted value, indicating that the low Q^2 behavior is not quite correct. In recent years, these VMD/dispersion relation approaches have been extended to include chiral perturbation theory^{118,119,120,121,122}. Mergell *et al.*¹¹⁸ obtained a best fit that gave an rms proton radius near 0.85 fm, closer to the accepted value of 0.86 fm, but could not do better when simultaneously fitting the neutron data. Hammer *et al.*¹¹⁹ included the available data on the form factors in the time-like region in the fit to determine the model parameters. These fits, also shown in Fig. 14, tend to under-predict the Jefferson Lab results at low Q^2 and over-predict at higher Q^2 , not being able to account for the slope. The latest work by Kubis¹²² which was restricted to the low Q^2 domain of $0 - 0.4 \text{ (GeV/c)}^2$, used the accepted proton rms radius of 0.86 fm as a constraint. The available data between Q^2 of 0.05 (GeV/c)^2

and 0.4 (GeV/c)^2 do not provide a severe test of the model, since they are limited by the uncertainties in the measurements of G_M^p in this region. However, Kubis' results show a marked departure from the trend of the Jefferson lab data as Q^2 increases, decreasing far too rapidly as shown in Fig. 14. This is not unexpected since their region of validity was claimed to be for $Q^2 \leq 0.4 \text{ (GeV/c)}^2$.

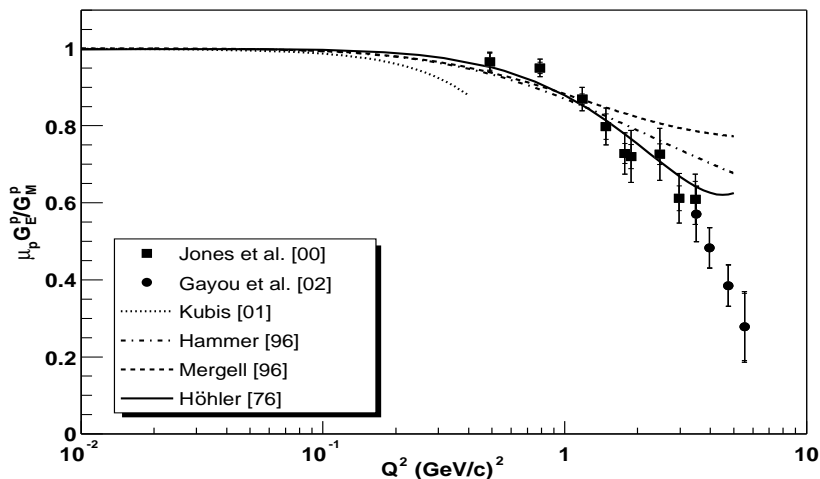


Fig. 14. Jefferson Lab data ^{56,58} on the proton form factor ratio, $\frac{\mu_p G_E^p}{G_M^p}$ as a function of Q^2 together with calculations from dispersion theory fits ^{117,118,119,122}.

Several authors have calculated the proton electric and magnetic form factors using various versions of the constituent quark model (CQM). Chung and Coester ¹²³, Aznauryan ¹²⁴, and Schlumpf ¹²⁵ all used a relativistic CQM (RCQM) to calculate nucleon form factors in the Q^2 range of 0 - 6 $(\text{GeV/c})^2$. Chung and Coester ¹²³ and Aznauryan ¹²⁴ were able to reproduce the then available data on $F_1^p(Q^2)$ and $F_2^p(Q^2)$ in the Q^2 range up to about 2 - 4 GeV^2 , above which the model deviated from the data particularly for Aznauryan. Schlumpf ¹²⁵ produced good agreement with later SLAC data showing a rise in the ratio of $\mu_p G_E^p / G_M^p$ which has now been shown to be contradictory with the recent Jefferson Lab results. More recent calculations have been made using the CQM in light front dynamics (LFCQM) by Cardarelli, Simula, Pace, and Salmè ^{126,127,99}. This approach uses a one-body current operator with phenomenological form factors for the CQs and light-front wave functions which are eigenvectors of a mass operator which reproduces a large part of the hadron spectrum. The $SU(6)$ symmetry breaking effects with and without the constituent quark form factor are also included. Their calculations reproduce the trend of the Jefferson lab results ^{56,58} reasonably well.

Frank, Jennings and Miller ¹⁰¹ have calculated the proton form factors in the

CQM (in light front dynamics using the model of Schlumpf¹²⁵) with the primary focus of investigating the medium modifications in real nuclei. Their results for the free proton are in reasonable agreement with the data to the highest Q^2 studied so far at Jefferson Lab and predict a change in sign of G_E^p at slightly higher Q^2 . Recently, this calculation was extended by Miller¹⁰⁷.

Li¹²⁸ used a relativistic quark model (RQM) in which symmetry is required in the center-of-mass frame. This has the effect of adding additional terms to the baryon wave function. The original wave function obtained before the $SU(6)$ symmetry requirement is constructed from spinors of quarks with zero momentum. The additional terms generated by the $SU(6)$ symmetry requirement are constructed from spinors of anti-quarks with zero momentum. Taken together with the original terms, these represent the inclusion of the sea quarks. The results of this calculation originally preceded the publication of the Jefferson Lab results⁵⁶, and the model gives good agreement with the data.

Ma, Qing and Schmidt¹²⁹ calculated the nucleon electromagnetic form factors within a simple relativistic quark spectator-diquark model using the light-cone formalism. Melosh rotations are applied to both quark and vector diquark. Their results describe the available experimental data well as shown Fig. 15. Recently, Wagenbrunn, Boffi, Klink, Plessas and Radici⁹⁸ calculated the neutron and proton electromagnetic form factors for the first time using the Goldstone-boson-exchange constituent quark model. The calculations are performed in a covariant framework using the point-form approach to relativistic quantum mechanics, and are shown in Fig. 15.

Another recent calculation of this type is from a perturbative chiral quark model (pChQM) by Lyubovitskij *et al.*¹³⁰. In this model, the effective Lagrangian describes relativistic quarks moving in a self consistent field, the scalar component of which provides confinement while the time component of the vector potential is responsible for short range fluctuations of the gluon field configurations, leading to a cloud of Goldstone bosons (π, K, η), as required by chiral symmetry. The results of these calculations drop much more rapidly than the experimental data. They also drop off more rapidly than either the results from the cloudy bag model (CBM), which uses a similar model, or those from the RCQM of Simula and co-workers.

Holzwarth has used a Skyrme/soliton model¹⁰⁰ to calculate the proton form factors and included loop corrections¹³¹. His results agree very well with the Jefferson Lab measurements. This results from a significant deviation of G_E^p below the “standard” dipole form. In fact, it is a general feature of these models that G_E^p changes sign for Q^2 somewhere larger than 5 GeV^2 (although exactly where is not well predicted), while G_M^p either does not change sign at all or does so at a very large value of Q^2 . They also agree very well with measured G_E^p and G_M^p values in the low Q^2 region and yield a proton rms radius of 0.869 fm, in close agreement with the currently accepted value.

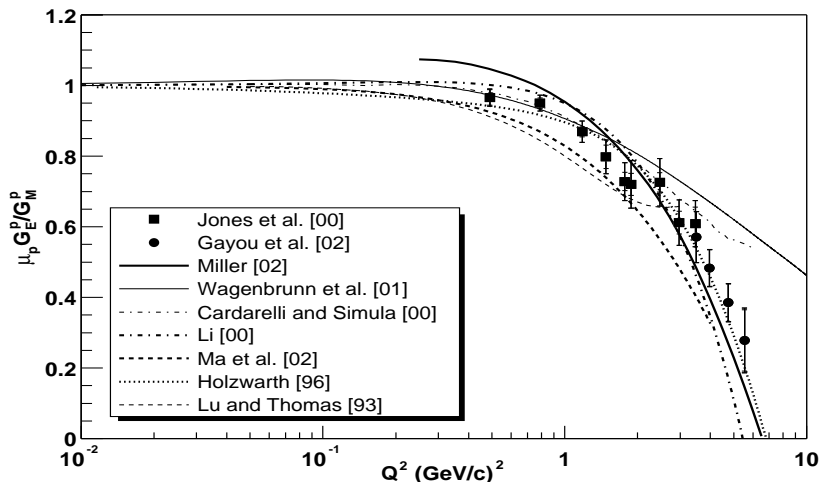


Fig. 15. Jefferson Lab data ^{56,58} on the proton form factor ratio, $\frac{\mu_p G_E^p}{G_M^p}$ as a function of Q^2 together with calculations from constituent quark models ^{99,107,100,128,134,98,129}.

In the MIT Bag Model, culminating in the so-called cloudy bag model (CBM) which includes the bare MIT bag plus a meson cloud, quarks are described as independent particles confined in a rigid spherical well. Such calculations have been performed by Lu and Thomas ^{132,133,134}. The introduction of the pion cloud improves the static properties of the nucleon by restoring chiral symmetry and also provides a convenient connection to πN and NN scattering. The result of these calculations is a ratio of G_E^p/G_M^p which decreases much more rapidly than indicated by the Jefferson Lab data. However, it provides a considerable improvement, as expected, over the bag model without the pion cloud which predicts a drop to zero at $Q^2 = 1.5 \text{ GeV}^2$ with a subsequent change of sign. The CBM calculation ¹³⁴ with a bag radius of 0.7 fm is also shown in Fig. 15, and the abrupt change of slope between 2 and 3 GeV^2 is inconsistent with the newer JLab results by Gayou *et al.* ⁵⁸.

In summary, the Soliton model calculation by Holzwarth ¹⁰⁰, the extended VDM model by Lomon ¹¹⁶, the relativistic CQM model calculation by Miller ¹⁰⁷, which is an improvement over its earlier version ¹⁰¹, and the relativistic quark spectator-diquark model calculation by Ma, Qing and Schmidt ¹²⁹, describe the new Jefferson Lab proton form factor ratio data very well. Fig. 16 shows the comparison between these models and the Jefferson Lab data ^{56,58}.

While it is important for a model to explain the observed Q^2 dependence of the proton form factor ratio, more stringent tests of the model can be provided by comparing calculations with data on all four nucleon form factors over the entire experimental accessible momentum transfer region. Fig. 17 shows the proton electric and magnetic form factor data published since 1970 obtained by the Rosenbluth

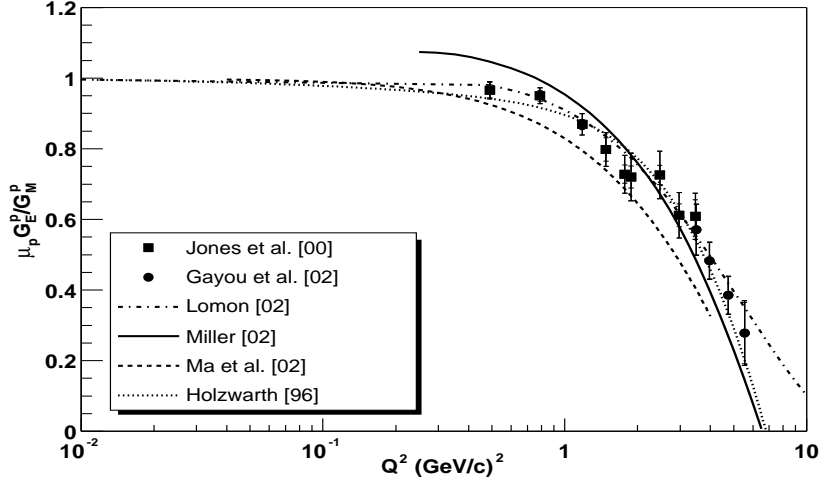


Fig. 16. Jefferson Lab data ^{56,58} on the proton form factor ratio, $\frac{\mu_p G_E^p}{G_M^p}$ as a function of Q^2 together with calculations by Lomon ¹¹⁶ (dash-dotted), Miller ¹⁰⁷ (solid curve), Holzwarth ¹⁰⁰ (dotted curve), and Ma, Qing, and Schmidt ¹²⁹ (dashed curve).

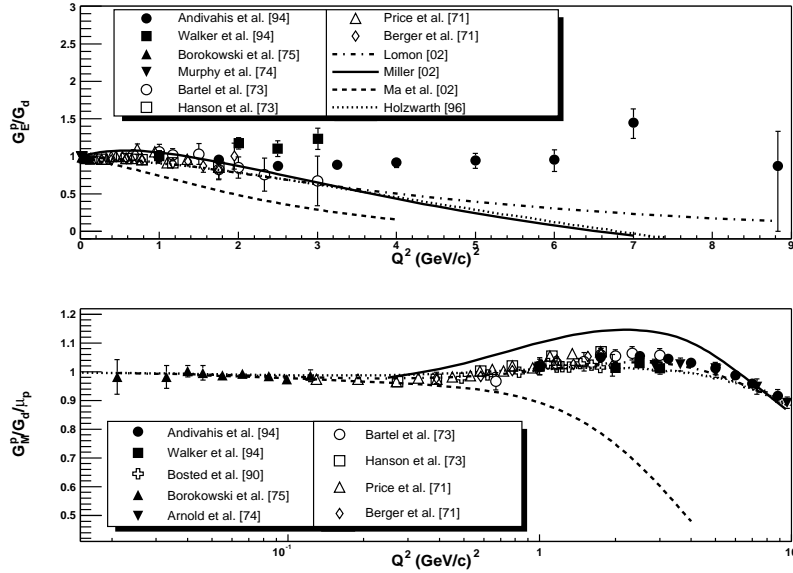


Fig. 17. World data on proton electromagnetic form factor, G_E^p and $\frac{G_M^p}{\mu_n}$ since 1970 in the unit of the standard dipole parameterization as a function of Q^2 together with calculations by Lomon ¹¹⁶ (dash-dotted), Miller ¹⁰⁷ (solid curve), Holzwarth ¹⁰⁰ (dotted curve), and Ma, Qing, and Schmidt ¹²⁹ (dashed curve).

method from unpolarized cross-section experiments, together with predictions from these models; Fig. 18 shows the corresponding neutron data and the model predictions. While most of the models are in good agreement with the proton magnetic form factor data, the departure of the model predictions from the G_E^p data at high Q^2 is not surprising. These models describe the trend of the Jefferson Lab proton form factor ratio data well, which are in disagreement with the proton form factor ratio formed by G_E^p and G_M^p obtained by the Rosenbluth separation method from unpolarized cross-section measurements. As shown in Fig. 18, none of these models are capable of describing the neutron electric and magnetic form factor data simultaneously in both the low Q^2 and high Q^2 region. While enormous theoretical progress has been made in recent years, significantly improved theoretical understanding the nucleon electromagnetic form factor is urgently needed.

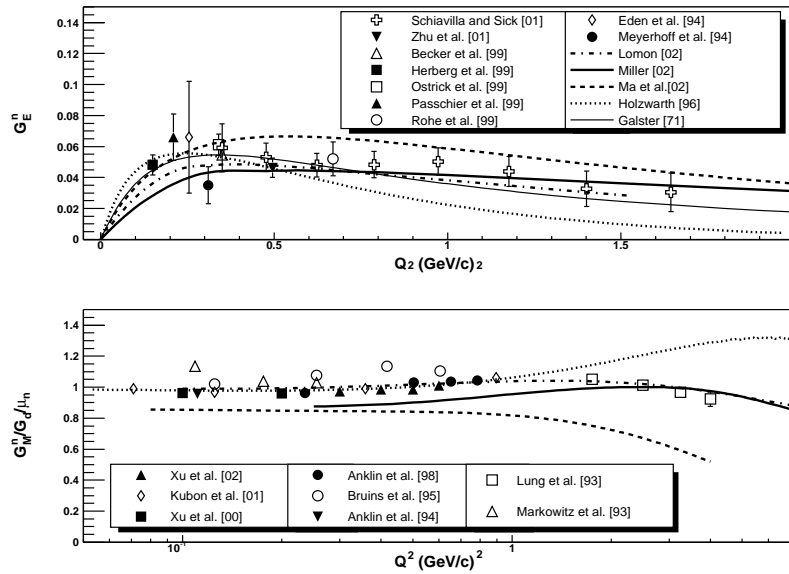


Fig. 18. World data on neutron electromagnetic form factor, G_E^n and $\frac{G_M^n}{G_M^p}$ since 1990 as a function of Q^2 together with calculations by Lomon¹¹⁶ (dash-dotted), Miller¹⁰⁷ (solid curve), Holzwarth¹⁰⁰ (dotted curve), and Ma, Qing, and Schmidt¹²⁹ (dashed curve).

6. Future Outlook

New, high precision data have been obtained in recent years from different electron accelerator laboratories around the world, thanks to new high luminosity facilities, and novel polarization experimental techniques. Future measurements extending into even higher momentum transfer region will be carried out in the near future, particularly with the planned energy upgrade of CEBAF to 12 GeV at Jef-

erson Lab ¹³⁵. With this upgrade, the proton form factor ratio measurement can be extended to a Q^2 value of 14 (GeV/c)² ¹³⁶. Such an extension will provide more stringent tests of various pQCD approaches discussed above. Furthermore, the neutron electric form factor measurement can be extended to a Q^2 value of 4 (GeV/c)² using the ${}^3\vec{H}e(\vec{e}, e'n)$ reaction ¹³⁷, and the neutron magnetic form factor measurement can be extended to a Q^2 value of about 10 (GeV/c)² employing the ratio technique of D(e,e'n)/D(e,e'p) ¹³⁸. This technique has been employed successfully recently using the CLAS detector at Jefferson Lab ³⁷.

Precision measurements of nucleon form factor in the low momentum transfer region, especially in the limit of $Q^2 \rightarrow 0$, which allows the determination of the nucleon electromagnetic radii, are equally important. This is a region where lattice QCD is anticipated to make reliable predictions in the near future and where effective field theories are expected to work. At MIT-Bates, the newly constructed BLAST detector will determine the nucleon electromagnetic form factor with high precision in the $Q^2 \leq 1.0(\text{GeV}/c)^2$ region using the novel experimental technique of scattering longitudinally polarized electrons in an electron storage ring from polarized internal gas targets with a large acceptance detector. The proton rms charge radius will be determined with much more higher precision from BLAST than from existing measurements from unpolarized electron-proton elastic scattering experiments. Such information will be sufficiently precise to allow high precision tests of QED from measurements of the hydrogen Lamb shift and equally importantly, will provide reliable tests of Lattice QCD calculations.

7. Acknowledgements

The author is grateful to many people for their help in the process of writing this paper. She would like to thank Drs. G. Holzwarth, X. Ji, B.A. Li, K.F. Liu, E. Lomon, B.Q. Ma, G.A. Miller, W. Plessas, I. Schmidt, S. Simula, A.W. Thomas, and R. Wagenbrunn for helpful discussions and for providing their calculations. She would like to thank her experimental colleagues: Drs. J.R. Calarco, O. Gayou, D. Higinbotham, R. Madey, A. Semenov, and I. Sick for their help. She is particularly indebted to Jason Seely for his tireless effort in maintaining the nucleon form factor data base, for making most of the figures in this article, and for careful reading of the manuscript. Finally, she thanks Dr. E.M. Henley for his valuable comments and suggestions. This work is supported by the U.S. Department of Energy under contract number DE-FC02-94ER40818 and DE-FG02-03ER41231. The author also acknowledges the Outstanding Junior Faculty Investigator Award (OJI) in Nuclear Physics from the U.S. Department of Energy.

1. F.J. Ernst, R.G. Sachs, and K.C. Wali, Phys. Rev. **119**, 1105 (1960).
2. R.G. Sachs, Phys. Rev. **126**, 2256 (1962).
3. S.J. Dong, K.F. Liu, and A.G. Williams, Phys.Rev. D **58**, 074504 (1998).
4. G.V. Dunne, A.W. Thomas and S.V. Wright, Phys. Lett. **B531**, 77 (2002).
5. L.N. Hand, D.G. Miller, and R. Wilson, Rev. Mod. Phys. **35**, 335 (1963).
6. G.G. Simon *et al.*, Nucl. Phys. **A333**, 381 (1980).

7. M. Weitz *et al.*, Phys. Rev. Lett. **72**, 328 (1994).
8. E.W. Hagley and F.M. Pipkin, Phys. Rev. Lett. **72**, 1172 (1994).
9. D.J. Berkeland, E.A. Hinds, and M.G. Boshier, Phys. Rev. Lett. **75**, 2470 (1995).
10. S. Bourzeix *et al.*, Phys. Rev. Lett. **76**, 384 (1996).
11. A. Van Wijngaarden *et al.*, Can. Journal of Phys. **76**, 95 (1998).
12. K. Melnikov and T. van Ritbergen, Phys. Rev. Lett. **84**, 1673 (2000).
13. S. Kopecky *et al.*, Phys. Rev. Lett. **74**, 2427 (1995).
14. N. Isgur, Phys. Rev. Lett. **83**, 272 (1999).
15. M.N. Rosenbluth, Phys. Rev. **79**, 615 (1950).
16. P. E. Bosted *et al.*, Phys. Rev. Lett. **68**, 3841 (1992); L. Andivahis *et al.*, Phys. Rev. D **50**, 5491 (1994); R. C. Walker *et al.*, Phys. Lett. **B 224**, 353 (1989); R. C. Walker *et al.*, Phys. Rev. D **49**, 5671 (1994); F. Borkowski *et al.*, Nucl. Phys. **B93**, 461-478,(1975); F. Borkowski *et al.*, Nucl. Phys. **A222**, 269-275 (1974); J.J. Murphy *et al.*, Phys. Rev. C **9**, 2125-2129 (1974); W. Bartel *et al.*, Nucl. Phys. **B 58**, 429 (1973); K.M. Hanson *et al.*, Phys. Rev. D **8**, 753-778 (1973); L.E. Price *et al.*, Phys. Rev. D **4**, 45-53 (1971); C. Berger *et al.*, Phys Lett. **35B**, 87-89,(1971); R. Arnold *et al.*, Phys. Rev. Lett. **57**, 174 (1986); A.F. Sill *et al.*, Phys. Rev. D **29** (1993); P.E. Bosted *et al.*, Phys. Rev. C **42**, 38 (1990); J. Litt *et al.*, Phys. Lett. **31B**, 40 (1970).
17. S. Platchkov *et al.*, Nucl. Phys. **A510**, 740 (1990).
18. M. Lacombe *et al.*, Phys. Rev. C **21**, 861 (1980).
19. M.M. Nagels, T.A. Rijken, J.J. de Swart, Phys. Rev. D **17**, 768 (1978).
20. R.B. Wiringa, R.A. Smith, T.L. Ainsworth, Phys. Rev. C **29**, 1207 (1984).
21. R.V. Reid, Ann. Phys. **50**, 411 (1968).
22. R. Schivilla, and I. Sick, Phys. Rev. C **64**, 041002-1 (2001).
23. E.B. Hughes *et al.*, Phys. Rev. **139**, B458 (1965); *ibid.* **146**, 973 (1966).
24. B. Grossetête, S. Jullian, and P. Lehmann, Phys. Rev. **141**, 1435 (1966).
25. A.S. Esaulov *et al.*, Sov. J. Nucl. Phys. **45**, 258 (1987).
26. R.G. Arnold *et al.*, Phys. Rev. Lett. **61**, 806 (1988).
27. A. Lung *et al.*, Phys. Rev. Lett. **70**, 718 (1993).
28. P. Stein *et al.*, Phys. Rev. Lett. **16**, 592 (1966).
29. W. Bartel *et al.*, Phys. Lett. **30B**, 285 (1969); *ibid.* **39B**, 407 (1972); Nucl. Phys. **B58**, 429 (1973).
30. P. Markowitz *et al.*, Phys. Rev. C **48**, R5 (1993).
31. R.J. Budnitz *et al.*, Phys. Rev. **173**, 1357 (1968).
32. K.M. Hanson *et al.*, Phys. Rev. D**8**, 753 (1973).
33. H. Anklin *et al.*, Phys. Lett. **B336**, 313 (1994).
34. E.E.W. Bruins *et al.*, Phys. Rev. Lett. **75**, 21 (1995).
35. H. Anklin *et al.*, Phys. Lett. **B428**, 248 (1998).
36. G. Kubon *et al.*, Phys. Lett. **B524** 26 (2002).
37. Jefferson Lab experiment E94-017, Spokespersons: W. Brook and M. Vineyard.
38. J. Jordan *et al.*, Proceedings of Workshop on Electron Nucleus Scattering, Elba 1998, editors: Benhar, Fabrocini, and Schivilla, p362.
39. T.W. Donnelly and A.S. Raskin, Ann. Phys. **169**, 247 (1986).
40. J. Kessler, *Polarized Electrons*, 2nd ed., Springer Series on Atoms and Plasmas, vol. 1 (Springer-verlag, New York, 1985).
41. R. Prepost and T. Maruyama, Annual Review of Nuclear Particle Science **45**, 41 (1995).
42. *Spin-exchange collisions and their consequences for spin-polarized gas targets of hydrogen and deuterium*, T. Walker and L.W. Anderson, Nuclear Instrument and Methods Phys. Res., Sec A **334**, 313 (1993); *Consequences of Spin-Exchange Collisions for Polarized Hydrogen and Deuterium Targets*, T. Walker and L.W. Anderson, Phys. Rev. Lett. **71**, 2346 (1993).

43. T.E. Chupp, R.J. Holt and R.G. Milner, *Annu. Rev. Part. Sci.* **45**, 373 (1994).
44. SMC (D. Adams *et al.*), *Phys. Lett.* **B329**, 399 (1994); SMC (A. Witzmann *et al.*), *Nucl. Phys.* **A577**, 319c (1994); SMC (D. Adams *et al.*), *Phys. Rev.* **D56**, 5330 (1997); SMC (B. Adeva *et al.*), *Phys. Lett.* **B412**, 414 (1997).
45. E143 (K. Abe *et al.*), *Phys. Lett.* **B364**, 61 (1995); E143 (K. Abe *et al.*), *Phys. Rev. Lett.* **74** 346 (1995).
46. E155 (G.S. Mitchell *et al.*), hep-ex/9903055.
47. R. DeVita *et al.*, *Phys. Rev. Lett.* **88**, 082001 (2002); Erratum **88**, 082001 (2002).
48. H. Zhu *et al.*, *Phys. Rev. Lett.* **87**, 081801, 2001.
49. D.G. Crabb and D.B. Day, *Nucl. Inst. and Meth. in Phys. Res.* **A356**, 9 (1995); T.D. Averett *et al.*, *Nucl. Inst. and Meth. in Phys. Res.* **A427**, 440 (1999).
50. M.W. McNaughton, *et al.*, *Nucl. Inst. Meth. in Phys. Res.* **A241**, 435 (1985); R.D. Ransome *et al.*, *Nucl. Inst. Meth.* **201**, 315 (1982).
51. O. Hausser *et al.*, *Nucl. Inst. and Meth* **A254**, 67 (1987).
52. B. Bonnin *et al.*, *Nucl. Inst. and Meth* **A288**, 379 (1990).
53. E. Aprile-Giboni *et al.*, *Nucl. Inst. and Meth* **215**, 147 (1983). D. Besset *et al.*, *Nucl. Inst. and Meth* **166**, 379 (1979).
54. B. Milbrath *et al.*, *Phys. Rev. Lett.* **80**, 452 (1998), *Phys. Rev. Lett.* **82**, 2221(E) (1999).
55. S. Dieterich *et al.*, *Phys. Lett.* **B500**, 47 (2001).
56. M. Jones *et al.*, *Phys. Rev. Lett.* **84**, 1398 (2000).
57. O. Gayou *et al.*, *Phys. Rev. C* **64**, 038202 (2001).
58. O. Gayou *et al.*, *Phys. Rev. Lett.* **88**, 092301 (2002).
59. A.I. Akhiezer and M.P. Rekalov, *Sov. J. Part. Nucl.* **3**, 277 (1974); R. Arnold, C. Carlson and F. Gross, *Phys. Rev. C* **23**, 363 (1981).
60. Jefferson Lab experiment E01-001, spokespersons: J. Arrington, and R. Segel.
61. MIT-Bates proposal 01-01, Spokespersons: J.R. Calarco, H. Gao, and H. Kolster.
62. T. Eden *et al.*, *Phys. Rev. C* **50**, R1749 (1994).
63. M. Ostrick *et al.*, *Phys. Rev. Lett.* **83**, 276 (1999).
64. C. Herberg *et al.*, *Eur. Phys. Jour.* **A5**, 131 (1999).
65. H. Arenhövel, *Phys. Lett. B* **199**, 13 (1987); *Z. Phys. A* **331**, 123 (1988).
66. Jefferson Lab experiment E93-038, spokespersons: R. Madey, S. Kowalski.
67. I. Passchier *et al.*, *Phys. Rev. Lett.* **82**, 4988 (1999).
68. B. Blankleider and R.M. Woloshyn, *nmPhys. Rev. C* **29**, 538 (1984).
69. J.L. Friar *et al.*, *Phys. Rev. C* **42**, 2310 (1990).
70. C. Ciofi degli Atti, E. Pace and G. Salme', *Phy. Rev. C* **46**, R1591 (1992); *Phy. Rev. C* **51**, 1108 (1995).
71. A. Kievsky, E. Pace, G. Salmè, M. Viviani, *Phys. Rev. C* **56**, 64 (1997), G. Salmè, private communication.
72. R.-W. Schulze and P. U. Sauer, *Phys. Rev. C* **48**, 38 (1993).
73. S. Ishikawa *et al.*, *Phys. Rev. C* **57**, 39 (1998).
74. J. Golak, G. Ziemer, H. Kamada, H. Witala, and W. Gloeckle, *Phys. Rev. C* **63**, 034006 (2001).
75. C.E. Woodward *et al.*, *Phys. Rev. Lett.* **65**, 698 (1990).
76. A. K. Thompson *et al.*, *Phys. Rev. Lett.* **68**, 2901 (1992).
77. M. Meyerhoff *et al.*, *Phys. Lett.* **B327**, 201 (1994).
78. H. Gao *et al.*, *Phys. Rev. C* **50**, R546 (1994); H. Gao, *Nucl. Phys.* **A631**, 170c (1998).
79. W. Xu *et al.*, *Phys. Rev. Lett.* **85**, 2900 (2000).
80. W. Xu *et al.*, *Phys. Rev. C.* **67**, R012201 (2003).
81. J. Golak *et al.*, *Phys. Rev. C* **51**, 1638 (1995).
82. D.O. Riska, *Phys. Scr.* **31**, 471 (1985).

83. J. Golak *et al.*, Phys. Rev. C **52**, 1216(1995); C.M. Spaltro *et al.*, Phys. Rev. Lett. **81**, 2870 (1998); W. Glöckle *et al.*, Electronuclear Physics with Internal Targets and the Blast Detector, edited by R. Alarcon and R.G. Milner, 185 (1999).
84. H.R. Poolman, Ph.D. Thesis, Vrije Universiteit Amsterdam (1999).
85. F. Xiong *et al.*, Phys. Rev. Lett. **87**, 242501 (2001).
86. J.-O. Hansen *et al.*, Phys. Rev. Lett. **74**, 654 (1995).
87. J. Golak, W. Glockle, H. Kamada, H. Witala, R. Skibinski, A. Nogga, Phys. Rev. C **65**, 044002 (2002).
88. J. Becker *et al.*, Eur. Phys. J. A **6**, 329 (1999).
89. D. Rohe *et al.*, Phys. Rev. Lett. **83**, 4257 (1999).
90. S. Galster *et al.*, Nucl. Phys. **B32**, 221 (1971).
91. H. Kamada, W. Glöckle, J. Golak, and Ch. Elster, Phys. Rev. C **66**, 044010 (2002).
92. X. Ji, Phys. Rev. Lett. **78**, 610 (1997); Phys. Rev. D **55**, 7114 (1997).
93. A.V. Radyushkin, Phys. Lett. **B380**, 417 (1996); Phys. Lett. **B385**, 333 (1996); Phys. Rev. D **56**, 5524 (1997).
94. S.J. Brodsky and G.R. Farrar, Phys. Rev. D **11**, 1309 (1975).
95. G.P. Lepage and S.J. Brodsky, Phys. Rev. D **22**, 2157 (1980).
96. A.V. Belitsky, X.D. Ji and F. Yuan, hep-ph/0212351.
97. E.L. Lomon, Phys. Rev. C **64**, 035204 (2001).
98. R.F. Wagenbrunn, S. Boffi, W. Klink, W. Plessas, M. Radici, Phys. Lett. B **511**, (2001) 33; e-print hep-ph/0108271.
99. F. Cardarelli and S. Simula, Phys. Rev. **C62** (2000) 065201; S. Simula, e-print nucl-th/0105024; S. Simula, private communication.
100. G. Holzwarth, Z. Phys. **A356** (1996) 339.
101. M. R. Frank, B.K. Jennings, G.A. Miller, Phys. Rev. **C54** (1996) 920.
102. K. Wijesooriya *et al.*, Phys. Rev. Lett. **86**, 2975 (2001).
103. K. Wijesooriya *et al.*, Phys. Rev. C **66**, 034614 (2002).
104. D. Abbott *et al.*, Phys. Rev. Lett. **84**, 5053 (2000).
105. S. Brodsky, hep-ph/0208158.
106. J.P. Ralston *et al.*, in Proc. of 7th International Conference on Interaction of particles and Nuclear Physics, Quebec City (2000), p. 302 (hep-ph/0206074); J.P. Ralston, P. Jain, hep-ph/0207129; hep-ph/0302043.
107. G.A. Miller, Phys. Rev. C **66**, 032201(R) (2002).
108. W. Detmold, W. Melnitchouk, J.W. Negele, D.B. Renner and A.W. Thomas, Phys. Rev. Lett. **87**, 172001 (2001); D.B. Leinweber, A.W. Thomas, K. Tsushima and S.V. Wright, Phys. Rev. D **61**, 074502 (2000); D.B. Leinweber, D.H. Lu and A.W. Thomas, Phys. Rev. D **60**, 034014 (1999).
109. E.J. Hackett-Jones, D.B. Leinweber and A.W. Thomas, Phys. Lett. B **494**, 89 (2000); V. Bernard, N. Kaiser and U. Meissner, Int. J. Mod. Phys. **E4**, 193 (1995).
110. M. Shifman, "Recent Progress in Heavy Quark Theory", lectures at TASI 95, published in *QCD and Beyond*, D.E. Soper (Ed.), World Scientific, 1996.
111. A.W. Thomas, private communication.
112. F. Iachello *et al.*, Phys. Lett. **B43** (1973) 191.
113. M. Gari and W. Krümpelmann, Z. Phys. **A322** (1985) 689.
114. M. Gari and W. Krümpelmann, Phys. Lett. **B274**, 159 (1992).
115. P.E. Bosted *et al.*, Phys. Rev. Lett. **68**, 3841 (1992); L. Andivahis *et al.*, Phys. Rev. **D50**, 5491 (1994).
116. E.L. Lomon, Phys. Rev. C **66**, 045501 (2002).
117. G. Höhler *et al.*, Nucl. Phys. **B114** (1976) 505.
118. P. Mergell *et al.*, Nucl. Phys. **A596** (1996) 367.
119. H.-W. Hammer *et al.*, Phys. Lett. **B385** (1996) 343.

120. Ulf-G. Meissner, Nucl. Phys. **A623** (1997) 340c.
121. Ulf-G. Meissner, Nucl. Phys. **A666 & 667** (2000) 51c.
122. B. Kubis and Ulf-G. Meissner, Nucl. Phys. **A679** (2001) 698.
123. P. L. Chung and F. Coester, Phys. Rev. **D44** (1991) 229.
124. I. G. Aznauryan, Phys. Lett. **B316** (1993) 391.
125. Felix Schlumpf, SLAC-PUB-6502 (1994), hep-ph/9405284.
126. F. Cardarelli *et al.*, Phys. Lett. **B357** (1995) 267.
127. E. Pace *et al.*, Nucl. Phys. **A666& 667** (2000) 33c.
(2000) 025208-1.
128. B.-A. Li, hep-ph/0004142 and private communication.
129. B.Q. Ma, D. Qing and I. Schmidt, Phys. Rev. C **65**, 035205, 2002; Phys. Rev. C **66**, 048201, 2002.
130. V. E. Lyubovitskij *et al.*, Phys. Rev. C **64** 065203 (2001).
131. G. Holzwarth, Nucl. Phys. **A666 & 667** (2000) 24c.
132. D. H. Lu *et al.*, Phys. Rev. **C57** (1998) 2628.
133. D. H. Lu *et al.*, J. Phys. G: Nucl. Part. Phys. **26** (2000) 175.
134. D. H. Lu *et al.*, Nucl. Phys. **A684** (2001) 296, and private communication.
135. "The Science Driving the 12 GeV Upgrade of CEBAF", an internal report of the Thomas Jefferson National Accelerator Facility, eds. L. Cardman, R. Ent, N. Isgur, J.-M. Laget, C. Leemann, C. Meyer, and Z.-E. Meziani (February 2001).
136. A. Saha, private communication.
137. B. B. Wojtsekhowski, private communication.
138. W. K. Brook, private communication.